UCLouvain

École polytechnique de Louvain

Numerical study of turbulent thermal convection in water pools

Author: **Alexandre PICARD**
Supervisor: **Miltiadis PAPALEXANDRIS**
Readers: **Julien CARLIER, Vincent LEGAT**
Academic year 2022-2023
Master [120] in Mechanical Engineering

Acknowledgement

First, I would like to thank my supervisor, Prof. Papalexandris Miltiadis, who supported and guided me throughout this thesis. I also thank him for his continuous availability and the encouragement he gave me.

I would also like to thank Dr Carlier Julien for helping me with the debugging of the code and the coding itself. His enthusiasm for numerical simulations and his constant availability are highly appreciated.

I thank Prof. Legat Vincent for reading my work.

Finally, I would like to express my gratitude to my family and friends who believed in me as well as in this thesis.

Abstract

Since the Fukushima disaster of 2011, there has been a growing interest in the scientific community to investigate the physical phenomena taking place in nuclear pools in order to improve their safety and prevent loss-of-cooling accidents that can lead to the release of a considerable amount of radioactive material. This thesis is part of this framework and aims to improve the understanding of evaporation-driven turbulent convection in spent fuel pools.

In this paper, the focus is on the thermal mixing of water below the interface of a spent fuel pool modelled as a cuboidal domain. To study this turbulent flow, a direct numerical simulation code written in C++ is employed. The effect of the airflow above the interface is modelled rather than simulated to estimate the evaporation rate at the interface. This work highlights the role of ambient temperature on mean flow properties and statistics and the influence of the aspect ratio on the emerging flow patterns.

Contents

1 Introduction

The fate of spent fuel, which is an inherent residue of the production of electricity by nuclear power stations, depends on national policies. The open cycle is implemented by such countries as Sweden and Finland, which consider spent fuel as waste and dispose of it in geological repositories. Others, such as France and Japan, perceive it as a potential resource that can be treated before being recycled; this is known as the closed cycle wherein only a tiny portion of the spent fuel is considered final waste [1] & [2].

Storage under water in spent fuel pools (SFPs) (illustrated in Figure 1.1) is always practised regardless of the chosen management strategy (recycling or not). This is also the case immediately following a reactor shutdown. Water effectively blocks radiation while allowing the efficient dissipation of the residual heat generation associated with the radioactive decay of the fission products and actinides contained in spent fuel rods [1]. These rods are stored in dedicated storage cells at the bottom of the pools for one to two years. All short-lived isotopes vanish, including iodin-131 and the majority of the activation products. The residual power decreases from 25 kW per tonne to around 7 kW per tonne in about two years [2].

Such pools must be constantly cooled by heat exchangers to maintain a safe temperature and avoid significant risks. Indeed, if the cooling system stops working or is not efficient enough, the heat dissipated by the rods can cause the water to boil and evaporate at an excessive rate, resulting in the exposure of the rods and the release of a considerable amount of radioactive substances. Moreover, as it heats up and upon contact with air, the zirconium in the cladding oxidises and can catch fire under the effect of the heat, increasing the risks of releasing radioactive elements and causing a natural disaster [2].

SFPs are typically made of reinforced concrete with a thickness of approximately 6 mm for structural purposes and to block radiation. They have a rectangular cross-section and are approximately 12 m deep. Spent fuel assemblies, which are composed of around 200 spent fuel rods (as shown in Figure 1.2a), are covered by approximately 7 m of water to provide sufficient protection for workers against ionising radiation during normal operations and to provide a reserve of water for cooling the assemblies in emergency cases. Spent fuel rods are placed vertically in storage racks to promote natural convection cooling, and they are spaced adequately to prevent criticality [1].

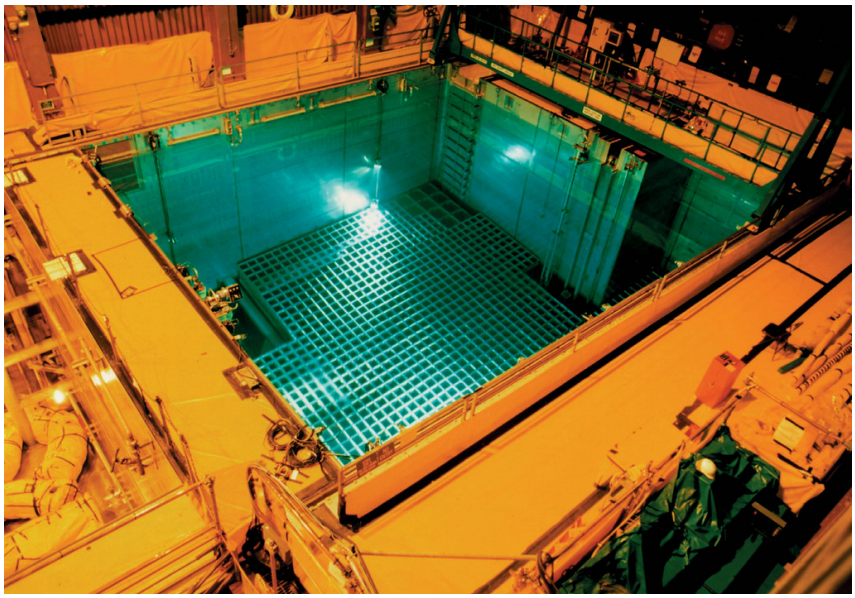

Figure 1.1: Typical spent fuel pool. [2]

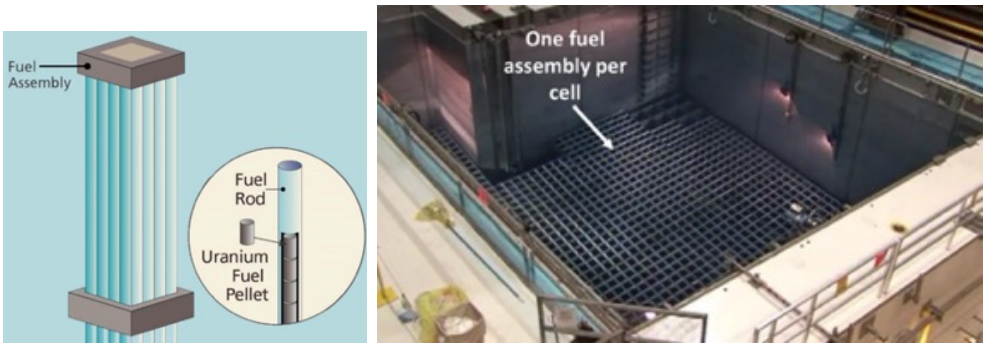

(a) (b)

Figure 1.2: Fuel assembly composition (a) and spent fuel pool cells (b) [3]

This thesis is focused on turbulent thermal convection driven by an evaporative free surface and aims to improve the knowledge of the operation of SFPs. Events such as Fukushima 2011 have shown that this topic is of great importance. On 11 March 2011, 14 nuclear power reactors of the four power stations located along the coast of Miyagi Prefecture in Japan were hit by a magnitude-9.0 earthquake and a tsunami [4]. Particular concern was expressed regarding Unit 4 of the Fukushima Daiichi reactor building where a loss-of-cooling accident occurred. Since there was no electricity, it was not possible to pump out the hot water and replace it with cold water. This accident could have led to a major release of radioactivity if the decrease in the water level had uncovered the fuel spent rods. To prevent such a scenario, external pumps were used to fill the SFP with seawater. It is worth noting that the impacted SFP close to the reactor had four times more radioactive material than the nuclear reactor core [4].

In the present study, direct numerical simulations (DNSs) are performed to investigate the role of the ambient temperature at two bottom wall temperatures, $T_{bot} = 315.25$ and $345.15\,\mathrm{K}$. For this purpose, four ambient temperatures from 289.15 K to 298.15 K with an increment of three are considered. The important mean flow properties, such as Ra, Nu,

Re and the evaporative mass flux $\dot{m}$" as well as flow statistics are presented, and data-fits provided. After that, the influence of the aspect ratio Γ, defined herein as the ratio of the domain length L to its height H: $\Gamma = \frac{L}{H}$ on LSC structures, is also studied. Three cuboidal domains are considered with $\Gamma = 1$, 2 and 4. The only dimension that varies is the domain's length, while the domain's height and width are kept constant. The diagonal and orthogonal planes are shown to visualise the influence of the aspect ratio on large-scale circulation (LSC) patterns thanks to the software Paraview.

This report is structured as follows; the second chapter presents the literature review. The third chapter is related to model development and is composed of the description of the domain, its boundary conditions, the governing equations and the evaporation model used to estimate the evaporation rates at the free surface. The fourth chapter presents the results of this study and the associated discussions. Finally, the fifth chapter outlines the conclusions drawn from this paper.

2 Literature review

2.1 Introduction

Turbulent thermal convection is a common turbulent flow type that occurs in nature, such as in the atmosphere, the planet's liquid core and stars. Turbulent thermal convection also plays a significant role in engineering applications in which heat transfer is involved and in industrial applications [5]. Thus, turbulent thermal convection investigation has attracted researchers' attention in different spheres, from mechanical engineering to geophysics and astrophysics [6].

Turbulent Rayleigh–Bénard convection has been a subject of interest and investigation in the thermal turbulence community for decades [7]. It is generally investigated as a fluid uniformly heated from below and cooled from above with solid lower and upper boundaries [8]. The system's geometry, the temperature differences across it and the resulting variations in fluid properties define the thermal dynamics and flow. The flow is governed by two dimensionless parameters, Rayleigh ($Ra = |g|\beta\Delta T H^3/(\nu k)$) and Prandtl ($Pr = \nu/k$), where $|g|$ signifies the gravitational acceleration magnitude, β corresponds to the thermal expansion coefficient, H means the domain's height, ν is the kinematic viscosity, ΔT relates to the difference that the upper and lower boundaries have in temperatures, and κ is the thermal diffusivity. The system response is evaluated in Reynolds and Nusselt numbers. The turbulent thermal evaporation-driven configuration is also characterised by the representative velocity – regarded as the LSC – which is formed across the domain's height and sweeps across the lower and upper boundaries. This phenomenon stabilises the thermal boundary layers and creates a hydrodynamic boundary layer with its shear [9].

2.2 Evaporation models

Scholars are working on creating and validating models that predict evaporation mass transfer rates across free surfaces in high-evaporation regimes. For most models developed before the Fukushima disaster of 2011, natural observations and measurements served as the base, such as evaporation at the ocean's surface. For example, Darwish (1998) used the Borelli–Sharif combination method (using the basic principles of thermodynamics, this method involves the calculation of turbulent heat flux transfer through the lower atmosphere) [10] to predict evaporation mass transfer rates at free water surfaces. His method required meteorological data and depended on wind profile interaction and aerodynamic roughness determination [11]. In these models, the mass transfer rate was inaccurately a bulk water temperature function and

accurately an ambient air conditions (temperature and relative humidity) function [9]. When developing models to predict the evaporation rates at the free surface, they did not consider that the mass transfer rate depends on the free surface temperature. Bulk and interfacial temperatures are different as a result of free surface evaporation, and, in a high mass transfer regime, this difference is more substantial [12]. The scholars conducted an experimental investigation of evaporation in tanks up to a maximum bulk temperature of 361.15 K under high mass transfer conditions. However, they did not distinguish between the bulk and free surface temperatures because the experimental techniques were limited [9].

After the Fukushima disaster, scholars started to develop new models to predict evaporation mass transfer rates across a free surface. Brewster presented a simple evaporation model with warm water pools with turbulent natural convection flow in the vapour phase. The proposed model can predict expected heat transfer and mass transfer behaviours even up to incipient boiling. These behaviours involve evaporative mass flux that rapidly increases and convective heat loss that rapidly declines as the pool temperature approaches the nuclear boiling point. The model is applicable to a low mass transfer rate regime as well as a high mass transfer rate regime [13].

The French Institut de Radioprotection et de Sûrete Nucléaire experimented with validating models to predict evaporation mass transfer rates across a free surface. The scholars tested the usage of insulated stainless steel tanks' sets of cuboidal and cylindrical shapes and different aspect ratios. After the tanks were heated and water-filled from below, they simultaneously measured mass and free surface temperatures, with an infrared camera measuring the latter. During the simulations, they recorded a high relative humidity and temperature on the experimental gadget. The experiment that the Institut de Radioprotection et de Sûrete Nucléaire conducted also concluded that the tanks' geometry did not significantly affect the evaporation rates when experimental error was considered [12].

Carlier and Papalexandris (2022) developed an algorithm to predict evaporation rates at free surfaces on collocated grids using a combination of the ghost fluid method and flux interpolation scheme. The algorithm is based on a low Mach number solver that uses a predictor-corrector time-marching scheme, with the ghost fluid method applied in the predictor and corrector stages. The algorithm was tested in both 2D and 3D configurations of turbulent thermal convection with evaporation across a free surface. The results showed that the algorithm can accurately predict the evaporative mass flux and free surface temperature, and can accurately compute the velocity, temperature field, and pressure of both phases in the simulation. In addition, the algorithm was able to resolve the turbulent flow structures near the free surface in 3D simulations, making it suitable for numerical treatment of gas-liquid flows with turbulent thermal convection and phase change through evaporation across a free surface [14].

2.3 Turbulent thermal convection simulations and experiments

Daya and Ecke (2001) conducted an experimental study of turbulent Rayleigh–Bénard convection in a cubic domain. The scholars measured vertical velocity fluctuations and temperature in cells with cylindrical and square geometries that had approximate unit aspect ratios. The

geometries had the same height and cross-sectional area. The experiment demonstrated that the velocity and temperature root mean square (RMS) quantities in the flow's bulk differed from those observed in the corresponding cylindrical domains with similar Pr and Ra. [15]. Amati *et al*. (2005) explored turbulent Boussinesq thermal convection in a cylindrical cell with an aspect ratio of $1/2$ and compared it with the results from previous experiments. Their simulation results spanned eight decades of Ra from $2 * 10^6$ to $2 * 10^{14}$ and formed the baseline data for a strictly Boussinesq fluid of constant Prandtl number. After experimenting, the scholars concluded that the Nusselt numbers ranged nearly from the $1/3$ power of Ra for four decades towards the upper end of the Ra range covered [16].

In turbulent Rayleigh–Bénard convection, the large scale circulation (LSC) can take different forms depending on the conditions of the system. At certain values of the Rayleigh number (Ra), Prandtl number (Pr), and aspect ratio (Γ), the LSC transitions from a single-roll state, in which it occupies the entire domain, to a dual-roll state. This occurs when the heat-carrying plumes driving the LSC become thick and lose their excess heat and buoyancy to the surrounding fluid before reaching the upper boundary. At this point, the LSC sinks to the middle of the domain to receive more heat from the lower boundary. [9].

In Marichal and Papalexandris' investigation, the large scale circulation (LSC) was stable for four time periods. The scholars used probes to record the time series of the vertical velocity component at specific points to determine these periods [17]. In other studies, the LSC also underwent reorientation during two different time-averaging periods: 400–500 t_{ff} and 400–1600 t_{ff}. In the first time period, the impingement point was located on the right, indicating that the LSC did not experience reorientation. During the second period, it changed position. However, the mean temperature profile did not experience significant changes, indicating that the LSC reorientation events did not significantly affect the mean temperature fields on the liquid and gas sides.

Hay and his colleagues conducted a study on turbulent thermal convection driven by free surface evaporation, in which the upper boundary surface area was fixed and the aspect ratio was varied through the height of the domain. In 3D cuboidal domains with an aspect ratio of $\Gamma = 1$ and a wide range of Prandtl numbers, the single-roll state of the large scale circulation (LSC) was found to dominate for about 90% of the time [9]. In cylindrical domains with an aspect ratio of $\Gamma = 1/2$ and water as the working fluid, the single-roll state also predominated for about 70% of the time [9]. However, in a study by Weiss and Ahler, the dual-roll state of the LSC was only observed during transitions between single-roll state reorientation events. At a smaller aspect ratio, specifically $\Gamma = 1/3$, the single-roll state is present for about 25% of the time, with the remainder being occupied by the LSC in the transition to or the dual-roll state [9]. This trend suggests that a further decrease in Γ reduces the likelihood of the single-roll state. This conclusion holds for both cuboidal and cylindrical domains. The single-roll state has been found to be effective for heat transfer in 3D geometries with water as the working fluid, leading researchers to study the aspect ratio, mean flow, evaporation rate, and statistics of the LSC in 3D geometries.

During the comparison between the DNS with LES velocity fluctuations' RMS predictions, the scholars noted a near parabolic profile with zero values at the boundaries. The profiles resemble those that Zikanov *et al*. obtained during their investigation of thermal convection setups under shear-free upper boundary conditions [18]. The scholars also observed a unique

hydrodynamic boundary layer at the lower wall and the maximum in-plane velocity fluctuations' RMS at the surface. The maximum bulk values for the DNS and LES match the vertical position where the counter-rotating circulations interact. This comparison demonstrated that the LES predictions were close to the DNS but slightly underestimated the peak in the domain's upper half [9]. The parabolic profile was not observed in Carlier and Papalexandris' investigation. According to their experiment's results, the temperature and velocity profiles near the free surface were smooth and did not have spurious oscillations [14]. In Marichal and Papalexandris' experiment, the profiles at the free surface were not symmetric with respect to the mid-height location. In particular, the values in the domain's upper half were lower than in the lower half at the free surface. This conclusion can also be referred to as the peaks near the boundaries. Based on the location of these peaks, the scholars noted that the upper thermal boundary layer was thinner compared with the lower boundary layer. The experiment also demonstrated that the values located in the bulk declined, and the thermal boundary layers became thinner when Ra increased. Regarding the reorientation events' impact, the scholars concluded that the profiles did not evolve due to the average time increase. They conclude similarly regarding the RMS of vertical velocity fluctuations [17].

3 Model development

3.1 Geometry and domain sizes

3.1.1 Two-dimensional geometry

The role of ambient conditions with regard to flow characteristics is studied based on a 2D model with a unit aspect ratio ($\Gamma = 1$), which corresponds to a square with a size of $L \times H$ (L and H stand for the domain length and height, respectively). In this paper, the domain length is maintained equal to the domain height: $H = L = 0.045$ m for all 2D cases.

3.1.2 Three-dimensional geometry

The role of the aspect ratio in the flow's characteristics is studied based on a cuboidal shape model with a varying aspect ratio with a size of $L \times W \times H$ (W stands for the domain width) and a varying aspect ratio Γ. The aspect ratio Γ of the cuboidal domain is defined as the ratio of the domain width W to its height H: $\Gamma = \frac{W}{H}$. The aspect ratio is only varied through the domain length, the domain height and width being constant: $H = W = 0.045\mathrm{m}$. This is to ensure a good comparison of the results, as the Rayleigh number is proportional to the cube of the characteristic length. As shown in Table 3.1, the investigated domains have an aspect ratio of 1, 2 and 4 and are 0.045, 0.09 and 0.18 m long.

Case	$L\,(\mathrm{m})$	$H\,(\mathrm{m})$	$W\,(\mathrm{m})$	$\Gamma\,(-)$
3D-DNS1	0.045	0.045	0.045	1
3D-DNS2	0.09	0.045	0.045	2
3D-DNS3	0.18	0.045	0.045	4

Table 3.1: Dimensions and aspect ratios of the investigated 3D domains.

3.2 Governing equations

In this study, the Navier–Stokes equations are solved directly to determine the turbulence effects on the flow in a DNS. As a very wide range of time and length scales have to be resolved down to the Kolmogorov scale in which turbulent kinetic energy is dissipated into heat, massive

computational resources are required. Thus, the ULiége cluster NIC5 dedicated to large parallel jobs is used to run the simulations developed in C++. The definitions of the Kolmogorov length, time and velocity scales are $\eta = \left(\frac{\nu^3}{\epsilon}\right)^{1/4}$, $\tau_\eta = \left(\frac{\nu}{\epsilon}\right)^{1/2}$ and $u_\eta = (\nu\epsilon)^{1/4}$, where ν stands for the kinematic viscosity of the fluid, and ϵ represents the average rate of dissipation of the turbulence's kinetic energy per unit mass, with units of m^2/s^3. The turbulent kinetic energy k is the mean kinetic energy per unit mass associated with eddies, and it is typically defined as half of the sum of the variances of the velocity components: $k = \frac{1}{2}\left(\overline{(u')^2} + \overline{(v')^2} + \overline{(w')^2}\right)$.

In the present study, the variations in density and transport properties along with temperature are taken into account, as the Oberbeck–Boussinesq approximation is not considered. Consequently, the system of equations corresponds to the low Mach number approximation of the compressible Navier–Stokes–Fourier equations:

$$\frac{\partial \rho}{\partial t} + \nabla \cdot (\rho \boldsymbol{u}) = 0, \tag{3.1}$$

$$\frac{\partial (\rho \boldsymbol{u})}{\partial t} + \nabla \cdot (\rho \boldsymbol{u}\boldsymbol{u}) = \nabla \cdot \boldsymbol{\tau} - \nabla p + \rho \boldsymbol{g}, \tag{3.2}$$

$$\frac{\partial \left(\rho c_p T\right)}{\partial t} + \nabla \cdot (\rho c_p \boldsymbol{u} T) = \nabla \cdot (\lambda \nabla T) + \frac{\mathrm{d}p_0(t)}{\mathrm{d}t}. \tag{3.3}$$

In equation (3.7), c_p stands for the specific heat, λ is the thermal conductivity and, as the studied domains are open, p_0 is equal to the ambient pressure. ρ corresponds to the fluid's density, and $\boldsymbol{u} = (u, v, w)$ stands for the fluid's velocity vector. τ represents the deviatoric part of the viscous stress tensor, and its definition is $\tau = \mu\left(\nabla \boldsymbol{u} + (\boldsymbol{\nabla u})^{\mathrm{T}} - \frac{2}{3}(\nabla \cdot \boldsymbol{u})\boldsymbol{I}\right)$, where $\boldsymbol{I}$ corresponds to the identity matrix, and μ is the dynamic viscosity.

A $\rho - T$ relation is used, as the governing equations must be closed by a water density isobaric 'equation of state'. This relation is obtained by fitting a four-order polynomial to the tabulated data from Lemon et al. [19]. The parameters λ and μ are also obtained from a quadratic polynomial fit.

A numerical algorithm from Antoniadis's thesis [20] for the treatment of the governing equations (3.5) and (3.5) is used. It is a generalisation of Lessani and Papalexandris's projection method for low Mach number Navier–Stokes equations in multiphase flows [21]. To improve stability and accuracy, a two-step advancement in time is used. With respect to spatial discretisation, second-order central difference schemes are used on a collocated grid, and, to prevent the odd–even decoupling of pressure, a flux interpolation technique based on Rhie and Chow (1983) [22] is employed.

3.3 Evaporation model

In this study, we employ Hay et al.'s (2021) dynamic evaporation model, which is efficient in terms of computation time, as it does not require multiple simulations. The Neumann thermal boundary condition, which is calculated at each time step, depends on the temperature of the cell closest to the interface and on fixed ambient conditions. These ambient conditions are varied in this study to determine their influences on flow properties and statistics. We determine the heat loss due to evaporation $\left(\dot{q}''_{\mathsf{evap}}\right)$ and convection $\left(\dot{q}''_{\mathsf{conv}}\right)$ at the water side of

the interface and use these values to apply a non-zero Neumann thermal boundary condition in the following form:

$$\frac{\partial \widetilde{T}}{\partial y} = \frac{1}{\lambda_{\text{int}}} \left(\dot{q}''_{\text{conv}} + \dot{q}''_{\text{evap}} \right) = \frac{1}{\lambda_{\text{int}}} \left(\dot{q}''_{\text{conv}} + \dot{m}'' h_{\text{lv}} \right), \tag{3.4}$$

where $\dot{m}''$ is the evaporative mass flux, h_{lv} is the latent heat of evaporation and $\lambda_{\text{int}}\, \partial \widetilde{T}/\partial y$ is the heat flux at the water side of the interface, with λ_{int} as the thermal conductivity of water at T_{int} .

Case	$T_\infty\,(\text{K})$	$p_0\,(\text{Pa})$	$\text{RH}\,(\%)$	$p_{\text{v},\infty}\,(\text{Pa})$	$\rho_\infty\,(\frac{\text{kg}}{m^3})$	$Y_{v,\infty}$	$Y_{a,\infty}$
DNS1	289.15	101325	40	730	1.22	0.0045	0.9955
DNS2	292.15	101325	40	880	1.2	0.0055	0.9945
DNS3	295.15	101325	40	1060	1.19	0.0066	0.9934
DNS4	298.15	101325	40	1270	1.18	0.0079	0.9921
DNS-RH1	298.15	101325	20	637	1.18	0.004	0.996
DNS-RH2	298.15	101325	30	955	1.18	0.0059	0.9941
DNS-RH4	298.15	101325	50	1591	1.17	0.0099	0.9901

Table 3.2: Properties of the gaseous mixture far from the interface. T_∞ and p_∞ correspond to the ambient temperature and pressure, respectively. RH is the relative humidity. $p_{v,\infty}$ and ρ_∞ signify the water vapour pressure and density of the gaseous mixture far from the interface, respectively. $Y_{v,\infty}$ and $Y_{a,\infty}$ are the vapour mass fraction and air mass fraction far from the interface, respectively. The values related to DNS5 to 8 are not provided, as they have the same ambient conditions as DNS1 to 4, and the ambient conditions of DNS-RH3 are identical to those of DNS4.

To determine the evaporative heat losses, the first step is to fix the gas-side conditions. Then, the water vapour partial pressure, $p_{v,\infty}$, is calculated using a Wagner equation and given as

$$p_v = p_c \exp\left(\left(a\tau + b\tau^{1.5} + c\tau^3 + d\tau^6 \right) / T_r \right), \tag{3.5}$$

where p_c and T_c are the critical pressure and temperature, respectively. $T_r = \widetilde{T}/T_c$ is the reduced temperature, and $\tau = 1\text{–}T_r$. Wagner's constants, a, b, c and d, can be found in the literature [23].

The vapour mass fraction far from the interface is obtained from

$$Y_v = \frac{p_v M_w}{p_v M_w + (p_0\text{–}p_v)\, M_a}. \tag{3.6}$$

The mass fraction of the air far from the interface can be expressed as $1\text{–}Y_{v,\infty}$. The molar masses of water and air are denoted by M_w and M_a, respectively. The density of the gaseous mixture far from the interface, ρ_∞, is calculated using the ideal gas equation of state:

$$\rho_g = \frac{M_w p_v}{RT} + \frac{M_a\,(p_0\text{–}p_v)}{RT}, \tag{3.7}$$

where ρ_g is the gaseous mixture's density, $R = 8314\ J/kmol/K$ is the universal gas constant, and T is the ambient temperature. The conditions at the interface are determined in

a similar way by using the local temperature at the interface to calculate the local saturation pressure $p_{v,\,\text{int}}$, the vapour mass fraction $Y_{V,\text{int}}$ and the mixture's density ρ_{int} .

In this model, it is assumed that there is a film of finite thickness that separates the conditions at the interface from those far away. The film's properties, such as its density (ρ_f) and dynamic viscosity (μ_f), are estimated based on the mean values of the conditions at the interface and far away. To determine the dynamic viscosity of the film, we use the kinetic theory of gases and consider a mixture of two components. The value of μ_f can be calculated using this formula:

$$\mu_f = \sum_{i=1}^{2} \frac{x_i \mu_i}{x_1 \phi_{i1} + x_2 \phi_{i2}}, \tag{3.8}$$

where x_i is the molar fraction of component i. The terms ϕ_{ij} are given by

$$\phi_{ij} = \frac{\left[1 + (\mu_i/\mu_j)^{1/2} (M_j/M_i)^{1/4}\right]^2}{\sqrt{8}\left[1 + (M_i/M_j)\right]^{1/2}}. \tag{3.9}$$

Here, μ_i and M_i are the dynamic viscosity and molar mass of component i, respectively. The dynamic viscosities of air and vapour can be found using polynomial fits. The film's kinematic viscosity v_f can then be calculated from the above values. The film's mass diffusivity for the binary mixture of air and vapour, D_f, is calculated using the following equation [24]:

$$D_f = 1.87 \times 10^{-10} \frac{T_f^{2.072}}{p_0} \left(\frac{m^2}{s}\right), \tag{3.10}$$

where p_0 is the thermodynamic pressure in units of atmospheres (i.e. equal to 1 atm). The film's diffusion coefficients are used to calculate the Schmidt number (Sc), and we use this to evaluate the concentration Rayleigh number (Ra_c) as follows:

$$Ra_c = \frac{|\boldsymbol{g}| (\rho_\infty - \rho_{int}) W^3}{D_f \mu_f}, \tag{3.11}$$

where W is the characteristic length scale (i.e. the width of the domain). To find the concentration boundary layer height (δ_c), we use a Sherwood number correlation for natural convection flows as follows [25]:

$$Sh = 0.23 Sc^{0.333} Ra_c^{0.321} \approx \frac{W}{\delta_c}. \tag{3.12}$$

The following equation is used to estimate the mass flux [26]:

$$\dot{m}'' = \frac{\rho_f D_f}{\delta_c} \log\left(1 + B_m\right), \tag{3.13}$$

where the mass transfer driving force B_m is defined as

$$B_m = \left(\frac{Y_{v,\infty} - Y_{v,int}}{Y_{v,int} - 1}\right). \tag{3.14}$$

Substituting this equation (3.14) into the equation for the mass flux (3.13) leads to the following relation:

$$\dot{m}'' = Sh\frac{\rho_f D_f}{W}\log\left(1+B_m\right). \tag{3.15}$$

Finally, we can find h_{lv} using a Watson relation [27],

$$h_{lv} = 2256.4\left(\frac{T_c – T_{int}}{T_c – 373.15}\right)^n, \tag{3.16}$$

with $n = 0.283$.

The rate of convective heat loss from the interface is proportional to the temperature difference between the interface T_{int} and the surrounding gaseous mixture at T_∞. This can be written as

$$\dot{q}''_{conv} = h\left(T_{int} – T_\infty\right). \tag{3.17}$$

The heat transfer coefficient h can be estimated using the following correlation for a horizontal flat surface that is warmer than the surrounding ambient air [28]:

$$\frac{hW}{\lambda_f} = Nu_t = 0.54\,Ra_t^{0.25}, \tag{3.18}$$

Finally, the film's thermal diffusivity κ_f is calculated using the aforementioned quantities, and the gas-side thermal Rayleigh number Ra_t is defined as

$$Ra_t = \frac{|\boldsymbol{g}|\beta_\infty\left(T_{int} – T_\infty\right)W^3}{\kappa_f \upsilon_f}. \tag{3.19}$$

3.4 Hypotheses, boundary conditions and initial conditions

3.4.1 Two-dimensional model

In the present study, the 2D turbulent flow beneath the interface of an SFP considered as a square domain of size $L \times H$ and filled with water at the ambient pressure of $p_0 = 101\,325$ Pa is investigated. The airflow above the evaporating free surface is not simulated. The gaseous mixture's properties far from the interface (at ∞) are included in Table 3.2. The interface surface level is kept constant; therefore, the mass loss due to evaporation is not modelled.

Dimensionless variables are introduced and denoted by a hat. The reference length is the height H, which is kept constant for all the investigated cases in this study. Free-fall time, which is an estimate of the time required for a local quantity of fluid set in motion by natural convection to travel the height of the domain, is defined as $t_{ff} = \frac{H}{U_{ff}}$ and obtained based on a reference velocity defined as $U_{ff} = \sqrt{gH\beta_{ref}\Delta T}$. The reference temperature is defined as $T_{ref} = \frac{T_{bot} – T_{int}}{2}$, where T_{bot} is the bottom wall temperature, and T_{int} is the interface temperature. The dimensionless temperature is defined as $\hat{\theta} = \frac{T – T_{ref}}{\Delta T}$ so that $-0.5 \leq \hat{\theta} \leq 0.5$, where $\Delta T = T_{bot} – T_{int}$.

The bottom wall located at $\hat{y} = 0$ has a fixed constant temperature, which means that the heat generated by the spent fuel rods is assumed to be uniform. A free-slip boundary

condition is applied to the top of the square domain located at $\hat{y} = 1$ to approximate a free surface: $\frac{\partial \hat{u}}{\partial \hat{y}}|_{\hat{y}=1} = 0$. The side walls of the domain located at $\hat{x} = 0$ and $\hat{x} = 1$ are considered adiabatic, with $\frac{\partial \hat{\theta}}{\partial \hat{x}}|_{\hat{x}=0}$ and $\frac{\partial \hat{\theta}}{\partial \hat{x}}|_{\hat{x}=1}$ prescribed. No-slip velocity boundary conditions are applied to the lower and side walls, as they are solid.

Three hydrodynamic boundary layers exist as a result of the boundary conditions mentioned above: one at each side wall and one at the lower wall. The thermal boundary layers are only present at the heated bottom wall and cooled upper boundary.

With respect to the initial conditions, the water is considered quiescent, and a linear temperature profile from the bottom wall temperature T_{bot} to the interface temperature T_{int} is assumed along the vertical direction.

The Rayleigh number is then provided by

$$Ra = \frac{g\beta_{ref}\left(T_{bot}–T_{int}\right)H^3}{\nu_{ref}\kappa_{ref}}, \tag{3.20}$$

where the kinematic viscosity ν_{ref} and thermal diffusivity κ_{ref} are calculated at the reference temperature T_{ref}.

3.4.2 Three-dimensional model

The hypothesis and initial conditions are identical to those developed for the 2D model in Subsection $3.4.1$. Regarding the boundary conditions, they can be easily extended from the 2D domain to the 3D domain. The major difference is that there are five hydrodynamic boundary layers instead of three as a result of the two extra vertical side walls, as the domain is cuboidal.

3.5 Resolution requirements

As stated previously, the Kolmogorov microscales of the flow have to be resolved everywhere to ensure the accuracy of the DNSs. The first requirement is to adequately resolve the hydrodynamic and thermal boundary layers in the vertical direction. At the Ra investigated, the boundary layers are considered laminar, as in the Prandtl–Blasius boundary layer theory. The dimensionless thermal boundary layers are obtained using the relation $\hat{\delta_\theta} = \frac{1}{2Nu}$ in all cases. The dimensionless hydrodynamic boundary layers $\hat{\delta_h}$ are obtained thanks to (3.21) and (3.24) for $Pr_{ref} > 3$ and < 3, respectively. The minimum number of cells in the hydrodynamic N_h and thermal N_θ boundary layers to satisfy the first requirement are calculated based on Shishkina *et al.*'s formulas [29] for $Pr_{ref} > 3$ (3.22 and 3.23), which is the case for DNS1 to 4, and for $Pr_{ref} < 3$ (3.25 & 3.26), which is the case for DNS5 to 8. To refine the mesh close to the walls, a hyperbolic tangent expansion function is employed.

$$\hat{\delta}_h = \frac{1}{2}\ E^{-1}\ Nu^{-1}\ Pr^{1/3}, \tag{3.21}$$

$$N_h = \sqrt{2}\ a\ E^{1/2}\ Nu^{1/2}\ Pr^{1/3}, \tag{3.22}$$

$$N_\theta = \sqrt{2}\ a\ E^{3/2}\ Nu^{1/2}, \tag{3.23}$$

where the empirical constants are $a = 0.482$ and $E = 0.982$, and,

$$\hat{\delta}_h = \frac{1}{2}\ Nu^{-1}\ Pr^{\Omega}, \tag{3.24}$$

$$N_h = \sqrt{2}\ a\ Nu^{1/2}\ Pr^{\chi}, \tag{3.25}$$

$$N_\theta = \sqrt{2}\ a\ Nu^{1/2}\ Pr^{\Psi}, \tag{3.26}$$

where $\Omega = 0.357$–$0.022\ logPr$, $\chi = 0.3215$+$0.011\ logPr$ and $\Psi =$ –0.0355+$0.033\ logPr$.

Ra	Pr_{ref}	$T_{bot}\,(\mathrm{K})$	$N_x \times N_y$	$\hat{\delta_h}$	$\hat{\delta_\theta}$	N_h	N_θ	$\hat{\Delta y}_{max}$	$\frac{\hat{\Delta y}_{max}}{\pi\eta_\theta}$
9.36 10^6	4.02	315.25	100×100	0.038	0.023	10 (5)	6 (3)	0.012	0.646
5.85 10^7	2.49	345.15	180×180	0.021	0.015	10 (6)	8 (4)	0.0096	0.714

Table 3.3: Resolution requirements for DNS1 ($Ra = 9.36\ 10^6$) and DNS5 ($Ra = 5.85\ 10^7$). Both simulations consider an ambient temperature of $T_\infty = 292.15\,\mathrm{K}$. In this table, T_{bot} is the bottom wall temperature, Ra is the Rayleigh number, Γ is the aspect ratio and $N_x \times N_y$ is the grid resolution in the x and y directions. Concerning N_h and N_θ, the true number of cells in the hydrodynamic and thermal boundary layers are presented, and the minimum number of cells needed to resolve these layers is in parenthesis. $\hat{\Delta y}_{max}$ is the largest dimensionless cell length in the y direction. The last column is the maximum ratio between the maximum cell length and the temperature microscale.

The second requirement is to resolve all eddies present in the bulk of the flow, where the turbulent fluctuations are assumed to be isotropic and homogeneous. To satisfy this requirement, a maximum cell size is defined based on the most stringent condition that is related to the temperature microscale, η_θ for fluids, with $Pr > 1$, which is the case for liquid water. This condition is expressed as an equality in the following form [30]:

$$\Delta \leqslant \pi\eta_\theta \approx \pi H \left(\frac{1}{Ra\ Pr\ Nu}\right)^{1/4}, \tag{3.27}$$

where Δ is the maximum cell length, H is the height of the domain and Nu is obtained thanks to a $Ra - Nu$ correlation from Hay (2021) in which the relation $Nu = 0.178 * Ra^{0.301}$ is found [9].

As shown in Table 3.3, the hydrodynamic and thermal boundary layers are all over-resolved by a factor of 2 for the DNS simulations except for the hydrodynamic boundary layer of DNS5, which is over-resolved by a factor of 1.67. The ratio between the maximum cell length and the temperature microscale is under 1 as well, which means that the eddies in the bulk of the

flow are also resolved. Only two simulations (DN1 and DNS5) lead to the highest Ra, which corresponds to the cases with the lowest ambient temperature ($T_\infty = 292.15\,\mathrm{K}$) for the two investigated lower wall temperatures ($T_{bot} = 315.25$ and $345.15\mathrm{K}$), are presented. These are the extreme cases, and all the requirements are satisfied for the remaining simulations to be presented in Chapter 3.3.

3.6 Convergence study

3.6.1 Convergence of the mean normalised temperature profiles

Since this paper is about the influences of the ambient conditions on the flow, it is necessary to obtain the Ra number and evaporative mass flux to characterise them, as the interface temperature plays a major role. It is also necessary to ensure that the mean normalised temperature $\langle\hat{\theta}\rangle_x$ profiles across the vertical direction converge in order to obtain consistent values. The extreme cases leading to the highest Ra are presented for the two bottom wall temperatures investigated, $T_{bot} = 315.25$ and $345.25\,\mathrm{K}$, at the lowest ambient temperature of $T_\infty = 289.15K$ (DNS1 and 5, respectively). Their profiles are presented over various free-fall time intervals in Figures 3.1 and 3.2, respectively.

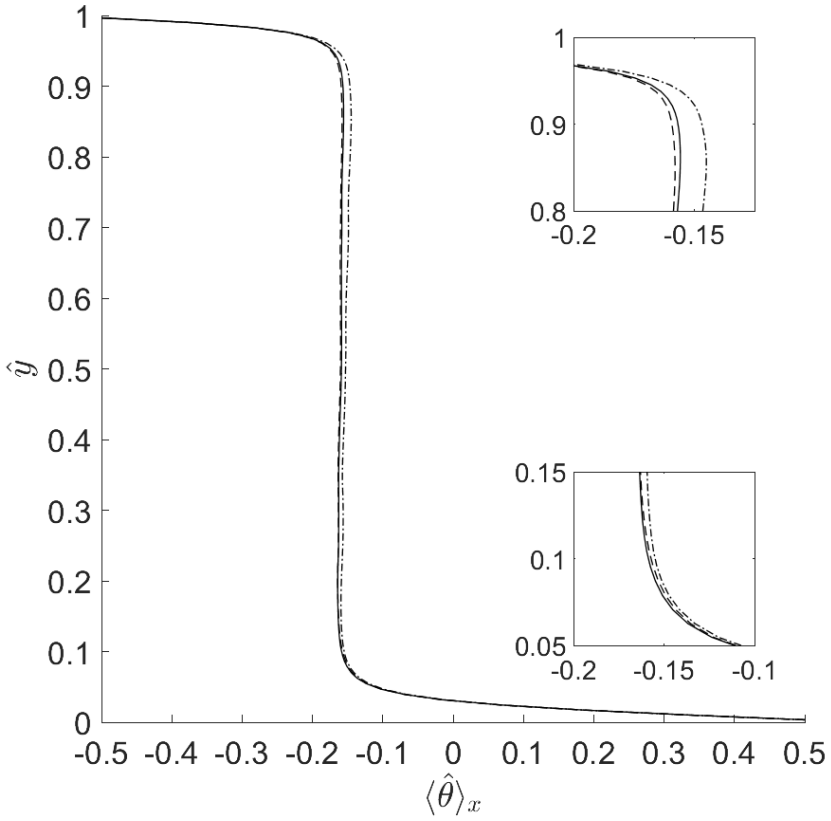

Figure 3.1: Plots of $\langle\hat{\theta}\rangle_x$ for DNS1 ($T_\infty = 292.15\,\mathrm{K}$ and $T_{bot} = 315.25\,\mathrm{K}$) over three free-fall time intervals: 200–$300\,t_{ff}$ $(-\cdot)$, 200–$400\,t_{ff}$ $(--)$, and 200–$500\,t_{ff}$ $(-)$. The top and bottom insets are zooms views of the upper and lower boundary layers, respectively.

The convergence study starts at $t_{ff} = 200$ because it has been shown that 100 t_{ff} are necessary to reach a statistically steady state [30], a higher free-fall time period is considered

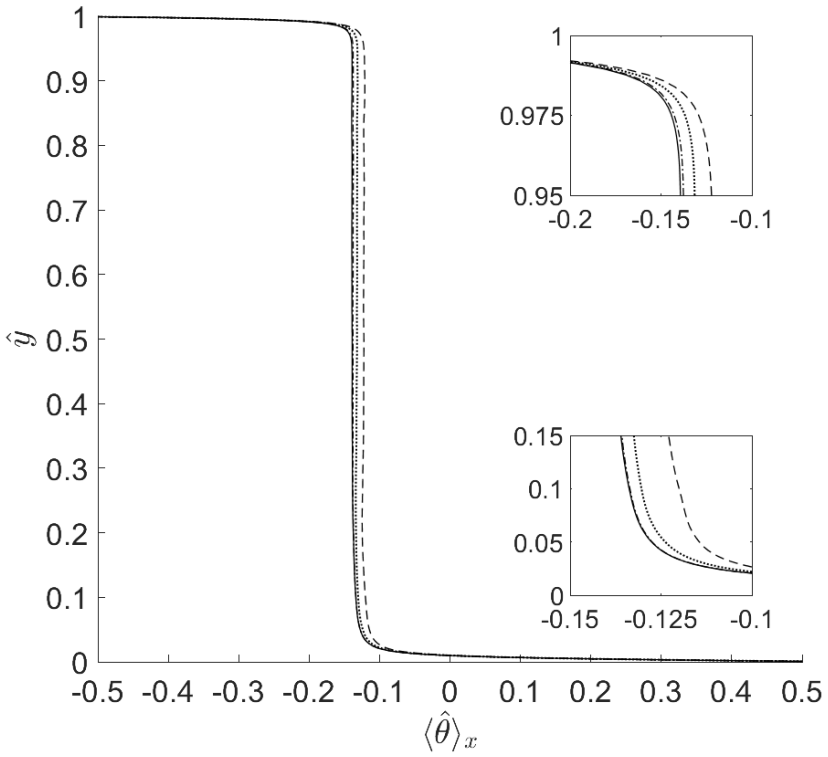

Figure 3.2: Plots of $\langle\hat{\theta}\rangle_x$ for DNS5 ($T_\infty = 292.15\,\mathrm{K}$ and $T_{bot} = 345.15\,\mathrm{K}$) and averaged over four free-fall time intervals: 200–$400\,t_{ff}$ $(-\cdot)$, 200–$600\,t_{ff}$ $(-)$, 200–$800\,t_{ff}$ $(--)$, and 200–$1000\,t_{ff}$ $(--)$. The top and bottom insets are zoomed views of the upper and lower boundary layers, respectively.

in order to be cautious. In Figure 3.1, it can be seen that the convergence of $\langle\hat{\theta}\rangle_x$ is achieved after a relatively short averaging time of 200 t_{ff}. The insets, which are the zoomed views of the profiles' bottom and top corners, allow us to assess the proper convergence of the two profiles corresponding to $200 - 400\,t_{ff}$ $(--)$ and $200 - 500\,t_{ff}$ $(-)$. It is worth noting that the interface's normalised temperature located at $\hat{y} = 1$ converges much more quickly than the normalised temperature of the bulk of the flow. This is reassuring, as it plays a key role in the following study.

Regarding DNS5 ($T_\infty = 292.15\,\mathrm{K}$ and $T_{bot} = 345.15\,\mathrm{K}$), the convergence of the $\langle\hat{\theta}\rangle_x$ profiles $\langle\hat{\theta}\rangle_x$ can be achieved only after a much longer averaging time compared with DNS1 ($T_\infty = 292.15\,\mathrm{K}$ and $T_{bot} = 315.25\,\mathrm{K}$). Indeed, it can be seen in Figure 3.2 that the profiles 200–$800\,t_{ff}$ $(--)$ and 200–$1000\,t_{ff}$ $(--)$ have converged. The inset zooms of the profiles' bottom and top corners are presented again to assess proper convergence. An average free-fall time of 600 t_{ff} is necessary to achieve a convergence of the profiles at the higher bottom wall temperature.

3.6.2 Convergence of the root mean square of the vertical velocity fluctuations profiles

As the dimensionless heat transfer characteristics of the flow are investigated in this paper, the convergence of the profiles of the RMS of the dimensionless vertical velocity fluctuations is

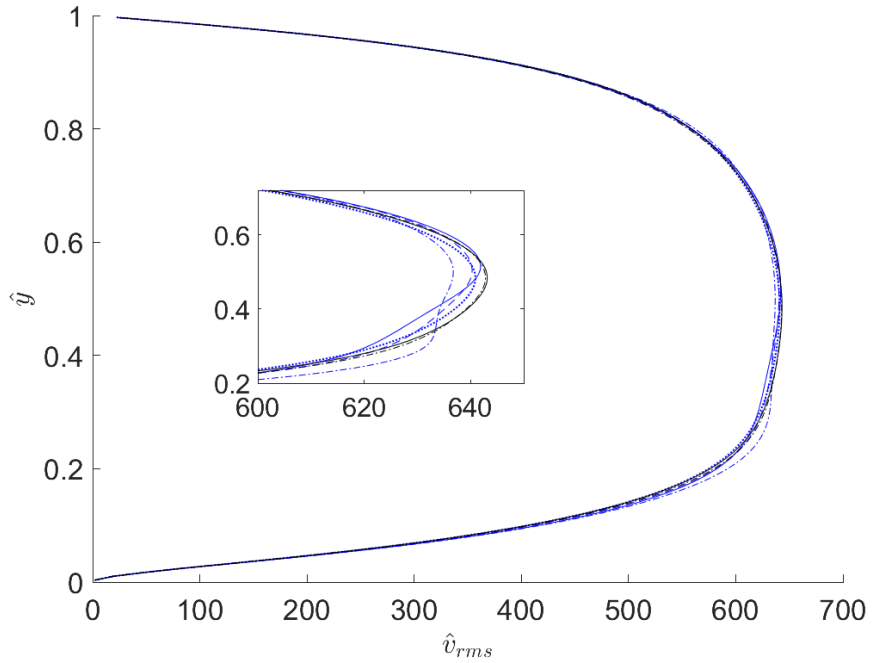

Figure 3.3: Plots of $\hat{v}_{rms}$ averaged over different free-fall time intervals for DNS1 ($T_\infty = 292.15\,\mathrm{K}$ and $T_{bot} = 315.25\,\mathrm{K}$): 200–$400\,t_{ff}$ $(-\cdot)$, 200–$600\,t_{ff}$ $(-)$, 200–$800\,t_{ff}$ $(--)$, 200–$1000\,t_{ff}$ $(\cdot\cdot)$, 200–$1200\,t_{ff}$ $(-\cdot)$, and $200-1400\,t_{ff}$ $(-)$. The inset is a zoomed view of the profiles for $600 \leq \hat{v}_{rms} \leq 653$.

examined, since it is involved in the calculation of the convective part of the Nusselt number, $Nu_{conv} = \sqrt{RaPr}\langle\hat{\rho}\hat{v}\hat{\theta}\rangle_x$. As in the previous section, the convergence study is performed for the extreme cases: DNS1 and 5. Their profiles are presented in Figures 3.3 and 3.4, respectively. The RMS of the vertical velocity is defined by $v_{rms} = \sqrt{\langle v'v'\rangle}$ and made dimensionless, as follows:

$$\hat{v}_{rms} = \frac{v_{rms}\, l_{ref}}{\nu_{ref}}, \tag{3.28}$$

where l_{ref} is the reference length and corresponds to the domain's height $H = 0.045\,\mathrm{m}$ for all simulations. The reference values are provided in Table 4.2.

In Figure 3.3, we can observe that the $\hat{v}_{rms}$ profiles present a significant asymmetry with respect to the domain centre for low free-fall time-averaging periods. This can be clearly seen in the 200–$400\,t_{ff}$ $(-\cdot)$ profile in the Figure 3.3 inset.

The $\hat{v}_{rms}$ profile continues to evolve as the averaging-time period increases, and its peak is shifted towards higher $\hat{y}$ for $(-\cdot)$, 200–$600\,t_{ff}$ $(-)$, 200–$800\,t_{ff}$ $(--)$ and 200–$1000\,t_{ff}$ $(\cdot\cdot)$. By continuing to increase the averaging time, the profile's peak is shifted closer to the domain mid and does not evolve after an averaging time of 1000 t_{ff}. This can be seen in the Figure 3.3 inset, where the profiles of 200–$1200\,t_{ff}$ $(-\cdot)$ and 200–$1400\,t_{ff}$ $(-)$ have entirely converged with a maximum relative discrepancy lower than 1% between them. The number of free-fall times considered for DNS1 to 4 is therefore 1000 t_{ff}, as this is more stringent than the convergence of the $\langle\hat{\theta}\rangle_x$ profiles, which require 200 t_{ff} only to converge.

This is repeated for the higher bottom wall temperature, and we can observe more signifi-

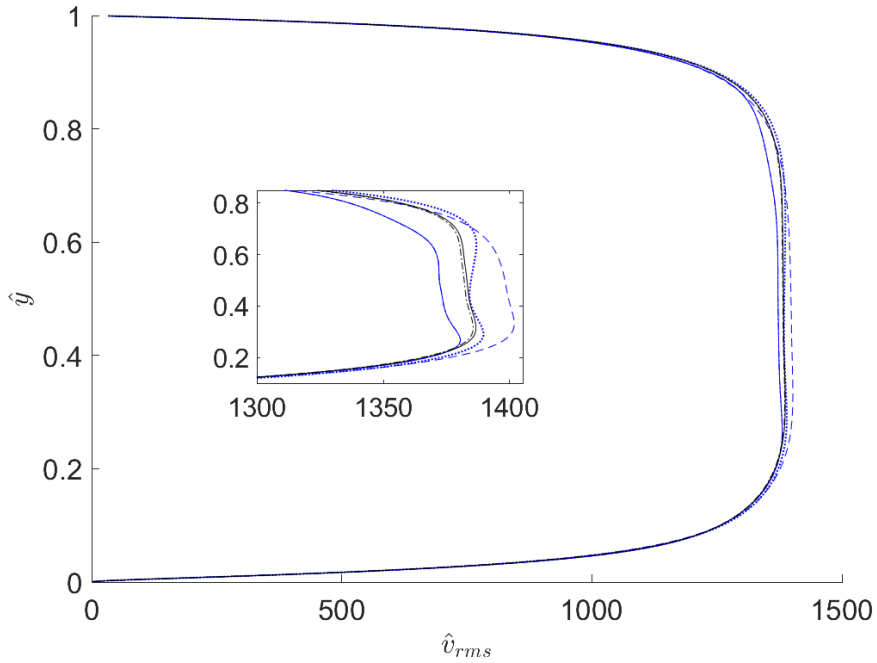

Figure 3.4: Plots of $\hat{v}_{rms}$ averaged over different free-fall time intervals for DNS5 ($T_\infty = 292.15\,\mathrm{K}$ & $T_{bot} = 345.15\,\mathrm{K}$): 200–400 t_{ff} $(-\cdot)$, 200–800 t_{ff} $(-)$, 200–1200 t_{ff} $(--)$, 200–1600 t_{ff} $(\cdot\cdot)$, 200–2000 t_{ff} $(-\cdot)$ and 200–2400 t_{ff} $(-)$. The inset is a zoomed view of the profiles for $1300 \leq \hat{v}_{rms} \leq 1400$.

cant fluctuations between the $\hat{v}_{rms}$ profiles for higher averaging free-fall time periods compared with the previous case, as seen in Figure 3.4. To achieve a relative discrepancy under 1%, 1800 t_{ff} is required for DNS5. The convergence of the profiles can be observed in the profiles of 200–2000 t_{ff} $(-\cdot)$ and 200–2400 t_{ff} $(-)$ in the inset of Figure 3.4. The number of free-fall times considered for DNS5 to 8 is therefore 1800 t_{ff}, which is more stringent than the convergence of the $\langle\hat{\theta}\rangle_x$ profiles that require 600 t_{ff} to converge.

4 Numerical results and discussion

4.1 The influence of the ambient temperature

The role of the ambient temperature at 2 bottom wall temperatures $T_{bot} = 315.25$ and $345.15\,\mathrm{K}$ on the flow is investigated. For this purpose, 4 ambient temperatures T_∞ are considered from 289.15 K to 298.15 K with an increment of 3 resulting in 8 simulations denoted DNS1 to DNS8, their results are presented in Table 4.1. This table includes the resulting Ra which is directly proportional to ΔT_w (the difference of temperature between the bottom wall and the interface T_{int}), the reference temperature T_{ref} and the evaporative mass flux $\dot{m}$" at the free surface. These results are plotted and fits are provided for the obtained data.

Case	Ra	Pr	$T_{bot}\,(\mathrm{K})$	$T_\infty\,(\mathrm{K})$	$T_{int}\,(\mathrm{K})$	$\Delta T_w\,(\mathrm{K})$	$T_{ref}\,(\mathrm{K})$	$\dot{m}$" $(\frac{\mathrm{g}}{\mathrm{m^2 s}})$
DNS1	9.36 10^6	2.49	315.25	289.15	312.55	2.7	313.9	0.281
DNS2	8.87 10^6	2.48	315.25	292.15	312.69	2.56	313.97	0.268
DNS3	8.42 10^6	2.48	315.25	295.15	312.82	2.43	314.04	0.252
DNS4	7.94 10^6	2.48	315.25	298.15	312.96	2.29	314.11	0.236
DNS5	5.85 10^7	2.49	345.15	289.15	337.36	7.8	341.25	1.5
DNS6	5.69 10^7	2.48	345.15	292.15	337.57	7.58	341.36	1.478
DNS7	5.61 10^7	2.48	345.15	295.15	337.67	7.48	341.41	1.453
DNS8	5.59 10^7	2.48	345.15	298.15	337.7	7.45	341.42	1.419

Table 4.1: Results of the simulations DNS1 to DNS8 related to the influence of the ambient and bottom wall temperatures on the flow properties.

Cases	$T_{ref,g}$ (K)	$\rho_{ref,g}$ $(\frac{\mathrm{kg}}{\mathrm{m^3}})$	$\beta_{ref,g}$ $(\frac{1}{\mathrm{K}})$	$v_{ref,g}$ $(\frac{\mathrm{m^2}}{\mathrm{s}})$	$\kappa_{ref,g}$ $(\frac{\mathrm{m^2}}{\mathrm{s}})$	$Pr_{ref,g}$	U_{ff} $(\frac{\mathrm{m}}{\mathrm{s}})$	l_{ref} (m)
DNS1-4	314.20	991.8	3.75 10^{-4}	6.37 10^{-7}	1.52 10^{-7}	4.19	0.019	0.045
DNS5-8	341.65	978.6	5.68 10^{-4}	4.21 10^{-7}	1.61 10^{-7}	2.62	0.042	0.045

Table 4.2: Nondimensionalization reference values. In this table, U_{ff} is the reference free-fall velocity and l_{ref} the reference length which is the domain height for all simulations.

4.1.1 Interface phenoma and Rayleigh number

To investigate the influence of the ambient temperature on the flow, the time- and line-averaged interface temperature is analysed first since the other studied quantities such as the evaporative mass flux depend on it. It is also necessary to obtain the interface temperature to calculate the reference temperature T_{ref} and Ra. Figure 4.1 shows the evolution of the interface temperature with respect of the ambient temperature at (a) $T_{bot} = 315.25$ K and (b) $T_{bot} = 345.15$ K. We observe from Figure 4.1(a) a linear relationship between the interface and ambient temperatures at the lower bottom wall temperature while the interface temperature increases in a nonlinear manner with increasing the temperature far from the interface T_∞ as it can be seen from 4.1(b), values of T_{int} are provided in Table 4.1 and associated linear and third order polynomial fits are presented in Eq. (4.1) and Eq. (4.2) for the lower and higher bottom wall temperatures, respectively. It will be discussed later that the 2D simulations are limited in taking into account the complex phenomena that really take place in 3D at the higher bottom wall temperature. Therefore, we cannot conclude about the non-linear evolution of the interface temperature with respect to the ambient temperature and there is no study on this topic to refer to. Consequently, it would be interesting in a future study to confirm or refute the non-linear evolution of T_{int} with respect of T_∞ at the higher bottom wall temperature by performing 3D DNS simulations.

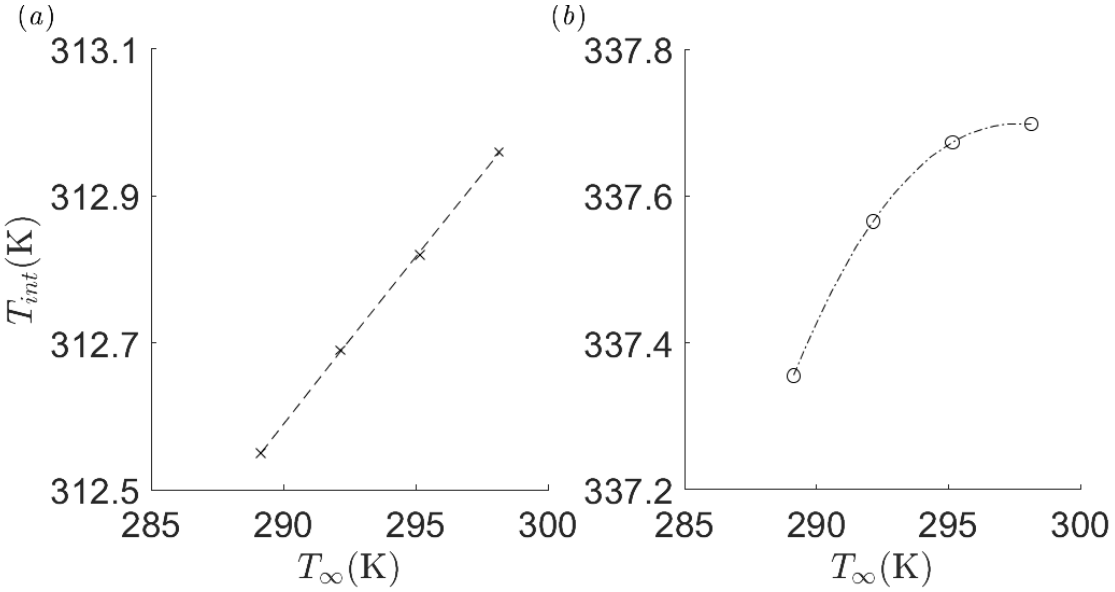

Figure 4.1: Plots of the interface temperature T_{int} with respect of the ambient temperature T_∞ at (a) $T_{bot} = 315.25$ K and (b) $T_{bot} = 345.15$ K with they respective fit $(--)$ and $(-\cdot)$.

$$T_{int} = 4.53 \times 10^{-2}\, T_\infty + 2.994 \times 10^{2}\,(\mathrm{K}), \tag{4.1}$$

$$T_{int} = a\, T_\infty^3 + b\, T_\infty^2 + c\, T_\infty + d, \tag{4.2}$$

where $a = 10^{-4}(\mathrm{K}^{-2})$, $b = -0.117\,(\mathrm{K}^{-1})$, $c = -35.9$ and $d = 3.33\,10^{3}\,(\mathrm{K})$.

We next obtain Ra by correcting the value provided by the code based on a first interface temperature guess leading to a first T_{ref} guess provided in Table 4.2 using Eq. (3.20) as we now have T_{int} and T_{ref}, the other parameters β_{ref}, ν_{ref} and κ_{ref} can obtained at T_{ref} but do

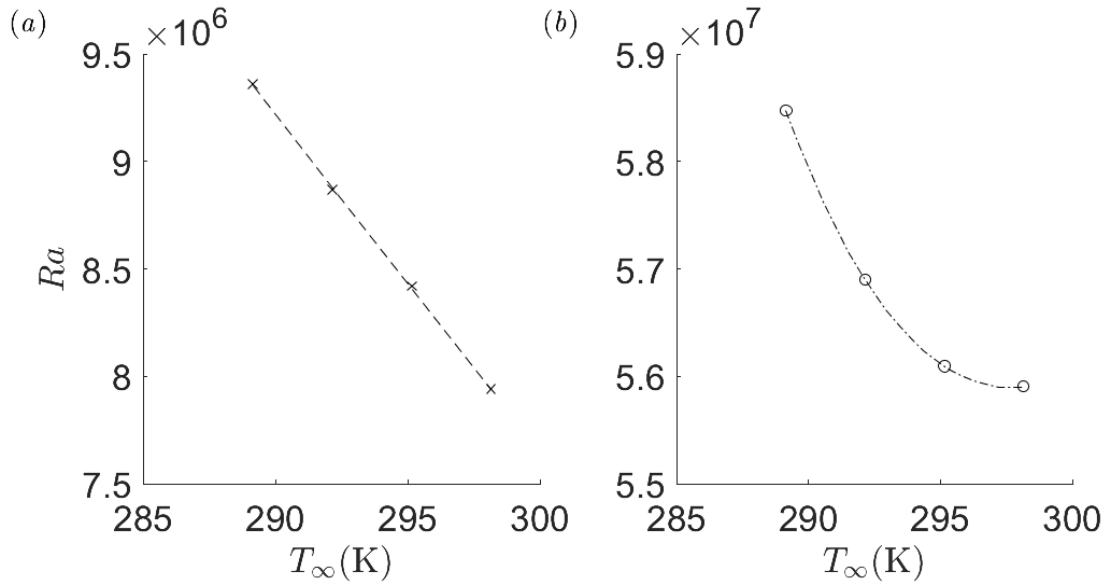

Figure 4.2: Plots of Ra with respect of the ambient temperature T_∞ at (a) $T_{bot} = 315.25$ K and (b) $T_{bot} = 345.15$ K with they respective fit $(--)$ and $(-\cdot)$.

not play a major role on the results as the interface temperature changes are relatively small. From Figure 4.2, it can be observed that Ra increases with reducing the ambient temperature in an inversely proportional way of the evolution of the interface temperature. The role of the ambient temperature on Ra is significant as shown in Table 4.1, there is a 18 % increase in Ra for $|\Delta T_\infty| = 9$ K from $T_\infty = 298.15$ K to 289.15 at the lower bottom temperature wall, this influence is less significant at the higher bottom wall temperature with an increase of Ra lower than 5 % considering the same variation of T_∞. But given what has been explained above about the 2D simulations limitations, one should be cautious about the results obtained regarding $T_{bot} = 345.15\,\mathrm{K}$. The associated linear and third order polynomial fits of Ra are presented in Eq.(4.3) and Eq.(4.4) for the lower and higher bottom wall temperatures, respectively.

$$Ra = -1.57 \times 10^5\,(\mathrm{K}^{-1})\,T_\infty + 5.475 \times 10^7, \tag{4.3}$$

$$Ra = a\,T_\infty^3 + b\,T_\infty^2 + c\,T_\infty + d, \tag{4.4}$$

where $a = -9.523\,10^2\,(\mathrm{K}^{-3})$, $b = 8.774\,10^5\,(\mathrm{K}^{-2})$, $c = -3\,10^8\,(\mathrm{K}^{-1})$ and $d = 3\,10^{10}$.

We next focus on the influence of the ambient temperature on the evaporative mass flux $\dot{m}$" which are obtained based on Hay et *al.*'s model developed in Section 3.3. This parameter is crucial in the case of spent fuel pool as previously explained the rods cannot be exposed to the surrounding air. The results are presented in Table 4.1 and plotted in Figure 4.3. Regarding the evaporative mass flux, we observe a linear relationship with respect of the ambient temperature for both bottom wall temperatures. The role of the ambient temperature on $\dot{m}$" is significant as shown in Table 4.1, there is a 27 % increase in $\dot{m}$" for $|\Delta T_\infty| = 9$ K from $T_\infty = 298.15$ K to 289.15 at the lower bottom temperature wall, this influence is again less significant at the higher bottom wall temperature with an increase of $\dot{m}$" lower than 6 % considering the same variation of T_∞.

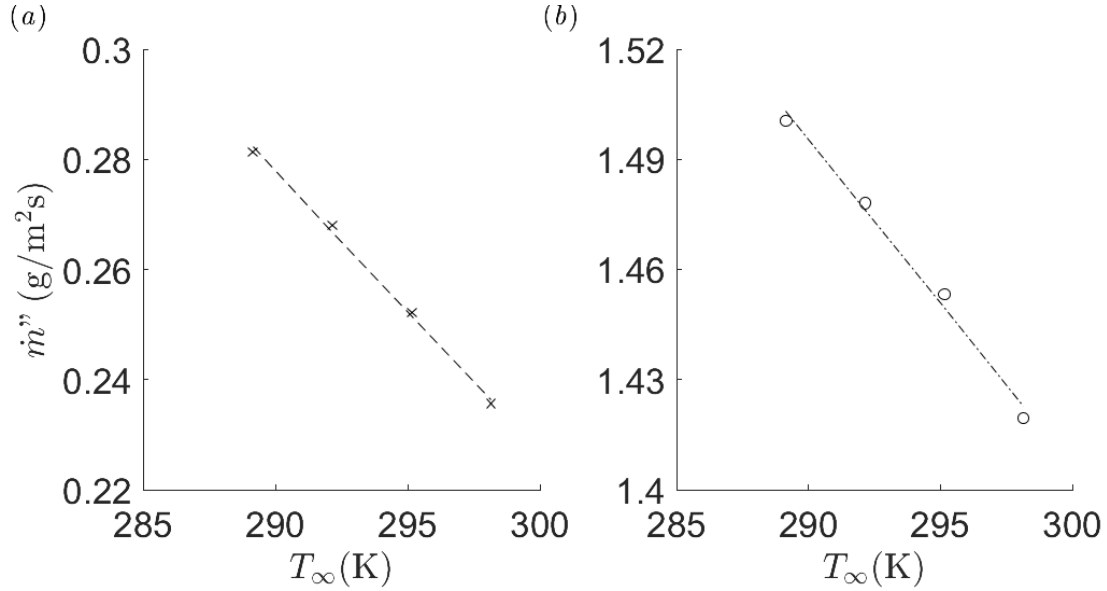

Figure 4.3: Plots of the evaporative mass flux $\dot{m}$" with respect of the ambient temperature T_∞ at (a) $T_{bot} = 315.25$ K and (b) $T_{bot} = 345.15$ K with their respective linear fit $(--)$ and $(-\cdot)$.

$$\dot{m}" = 5.097 \times 10^{-3} \, (\frac{\mathrm{g}}{\mathrm{K\,m^2s}}) \, T_\infty + 1.756 \, (\frac{\mathrm{g}}{\mathrm{m^2s}}), \tag{4.5}$$

$$\dot{m}" = 8.93 \times 10^{-3} \, (\frac{\mathrm{g}}{\mathrm{K\,m^2s}}) \, T_\infty + 4.085 \, (\frac{\mathrm{g}}{\mathrm{m^2s}}). \tag{4.6}$$

4.1.2 Heat transfer characteristics

To assess the role of the ambient temperature on dimensionless heat transfer characteristics, the local time- and line- averaged Nusselt number Nu_y and its convective and diffusive components: Nu_{conv} and Nu_{diff} are obtained and their evolution accross $\hat{y}$ showed in Figures 4.4 and 4.5 at $T_{bot} = 315.25$ K and $T_{bot} = 345.15$ K, respectively. The local Nusselt number Nu_y is defined as:

$$Nu_y = \underbrace{\sqrt{RaPr}\langle\hat{\rho}\hat{v}\hat{\theta}\rangle_x}_{Nu_{conv}} + \underbrace{\left\langle \hat{\lambda}\frac{\partial\hat{\theta}}{\partial\hat{y}} \right\rangle_x}_{Nu_{diff}}. \tag{4.7}$$

The global Nusselt number Nu is the averaged value over the 2D domain and is expressed by the given equation:

$$Nu = \sqrt{RaPr}\langle\hat{\rho}\hat{v}\hat{\theta}\rangle_{xy} + \left\langle \hat{\lambda}\frac{\partial\hat{\theta}}{\partial\hat{y}} \right\rangle_{xy}. \tag{4.8}$$

The flat profiles of Nu_{conv} showed in Figures 4.4(a) and 4.5(a) within the bulk of the flow indicate statistically stationary solutions for all simulations. It was ensured in the convergence study presented in Section 3.6. The major contribution to Nu within the bulk of the flow is the convective component of Nu while near the walls, it is the diffusive component which is responsible of the major contribution. From the Figure 4.4, we observe that the convective

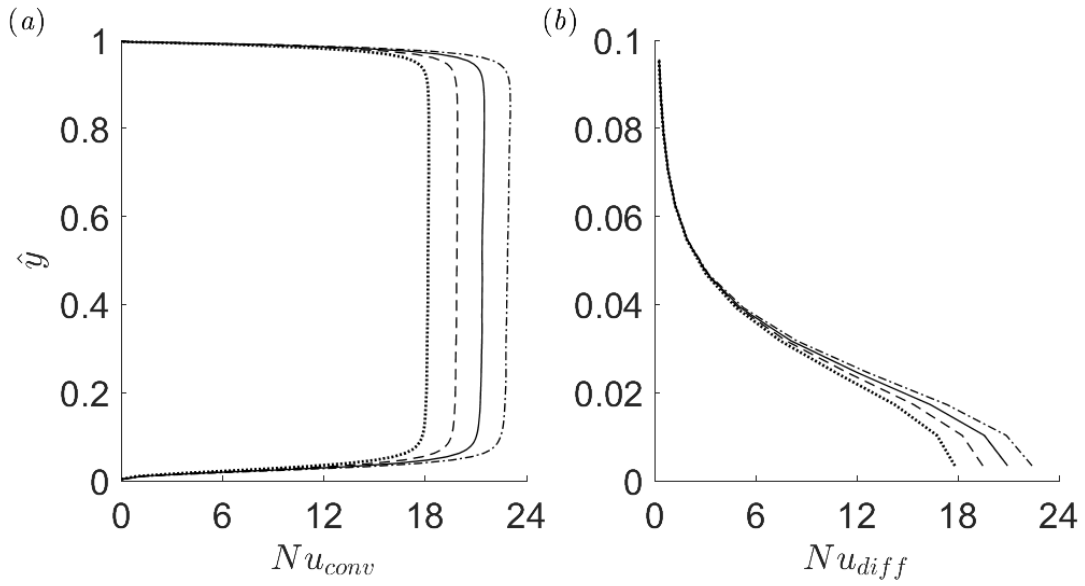

Figure 4.4: Plots of the time- and area averaged of (a) Nu_{conv} and (b) Nu_{diff} at $T_{bot} = 315.25\,\mathrm{K}$ and for 4 ambient temperatures: $T_\infty = 289.15\,(-\cdot)$, $292.15\,(-)$, $295.15\,(--)$ and $298.15\,(\cdot\cdot)\,\mathrm{K}$.

Nusselt profiles are shifted to the right while decreasing the ambient temperature. Therefore the global Nu is impacted in a similar way, the global Nusselt number values are included in Table 4.3 and decreases linearly with the increase of the ambient temperature as shown in Figure 4.6(a). There is a 26 % increase in Nu for $|\Delta T_\infty| = 9$ K from $T_\infty = 298.15\,\mathrm{K}$ to 289.15 K. A linear $Nu - T_\infty$ correlation is obtained and provided in Eq. (4.9). At the higher bottom wall temperature, the Nu components profiles are impacted by the limitations of the 2D simulations as explained previously. We observe from Figure 4.5(b) that the Nu_{diff} present similar behaviour close to domain's boundaries the for the following pairs: $T_\infty = 289.15\,(-\cdot)$ & $298.15\,(\cdot\cdot)\,\mathrm{K}$ and $T_\infty = 292.15\,(-)$ & $295.15\,(--)\,\mathrm{K}$ but a clear distinction within the bulk of the flow can be seen and suggest that the limitations of the 2D simulations impact the near wall regions mainly. Since the global Nusselt number is mainly the result of the convective contribution within the bulk of the flow, coherent values are obtained for the latter at the higher bottom wall temperature. It is also worth noting that for a higher bottom wall temperature, the convective Nusselt profiles are closer to each other than at the lower temperature. This shows that at a higher bottom wall temperature, the heat transfer characteristics are affected in a lesser extent by the ambient temperature with a 8 % increase in Nu for $|\Delta T_\infty| = 9$ K from $T_\infty = 298.15$ K to 289.15 which is 3.5 less important compared the lower bottom wall temperature. A linear $Nu - T_\infty$ correlation is also obtained and provided in Eq. (4.10). Figure 4.5(b)'s inset shows that in the near bottom wall region, the Nusselt diffusive component profiles appear in an expected order as $Nu_{conv}|_{\hat{y}\approx 0}$ increases with decreasing T_∞.

$$Nu_{y,T_1} = -0.5198\,(\mathrm{K}^{-1})\,T_\infty + 173, \tag{4.9}$$

$$Nu_{y,T_2} = -0.2803\,(\mathrm{K}^{-1})\,T_\infty + 116. \tag{4.10}$$

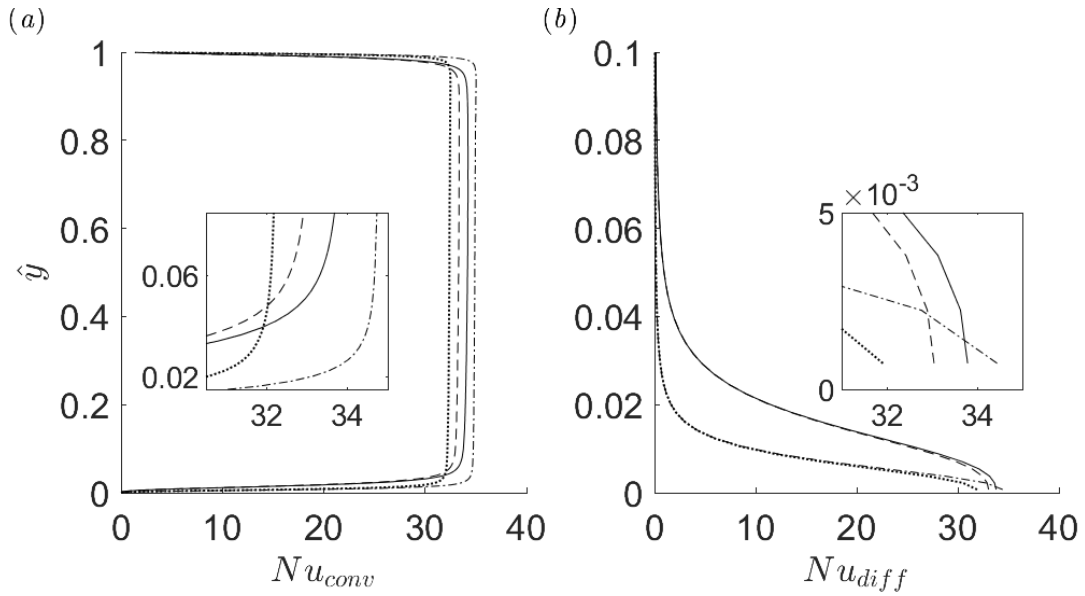

Figure 4.5: Plots of the time- and area averaged of (a) Nu_{conv} and (b) Nu_{diff} at $T_{bot} = 345.15\,\mathrm{K}$ and for 4 ambient temperatures: $T_\infty = 289.15\,(-\cdot)$, $292.15\,(-)$, $295.15\,(--)$ and $298.15\,(\cdot\cdot)\,\mathrm{K}$.

Case	$T_{bot}\,(\mathrm{K})$	$T_\infty\,(\mathrm{K})$	Nu	Case	$T_{bot}\,(\mathrm{K})$	$T_\infty\,(\mathrm{K})$	Nu
DNS1	315.25	289.15	22.66	DNS5	345.15	289.15	34.9
DNS2	315.25	292.15	21.18	DNS6	345.15	292.15	34.08
DNS3	315.25	295.15	19.65	DNS7	345.15	295.15	33.26
DNS4	315.25	298.15	17.97	DNS8	345.15	298.15	32.37

Table 4.3: Global Nusselt numbers Nu for DNS1 to 8.

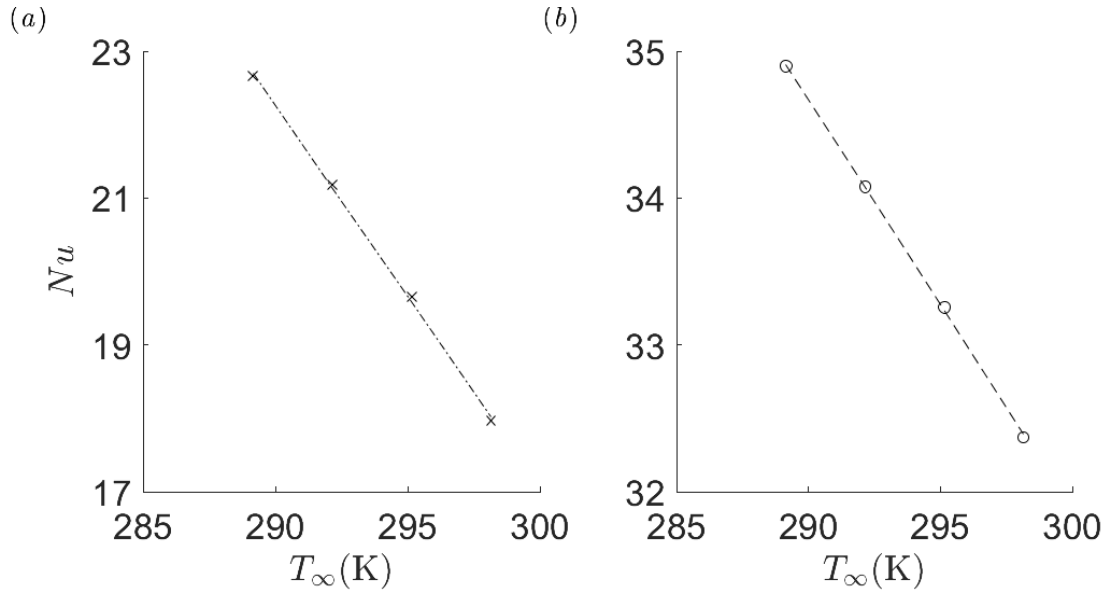

Figure 4.6: Plots of Nu with respect of the ambient temperature T_∞ at (a) $T_{bot} = 315.25$ K and (b) $T_{bot} = 345.15$ K with their respective linear fit $(-\cdot)$ and $(--)$.

4.1.3 Flow statistics

We first present $\langle\hat{\theta}\rangle_x$ profiles for the lower and higher bottom wall temperatures in Figures 4.7 and 4.8, respectively. The profiles show that the normalised temperatures at the centre of the flow which is about $\langle\hat{\theta}\rangle_{x,ctr} = -0.17$ and about $\langle\hat{\theta}\rangle_{x,ctr} = -0.14$ for the four profiles at $T_{bot} = 315.25$ K and $T_{bot} = 345.15$ K, respectively. In both cases, they are inferior than the mean $\langle\hat{\theta}\rangle_{mean} = 0$, that indicates that the profiles are shifted towards the cold interface temperature and in a lesser extent when the bottom wall temperature is increased. Moreover, the temperature drop between the bottom wall and the bulk of the flow is about twice the temperature drop between the bulk of the flow and the free surface temperature similarly as in [9]. The top and bottom insets in the Figures 4.7 and 4.8 are zooms of the linear regions inside the upper and lower thermal boundary layers, respectively. It is interesting to note that the profiles appear in an expected order with respect to their associated Ra, zooms of the profiles' corners are not showed as they don't allow to see a clear distinction between them.

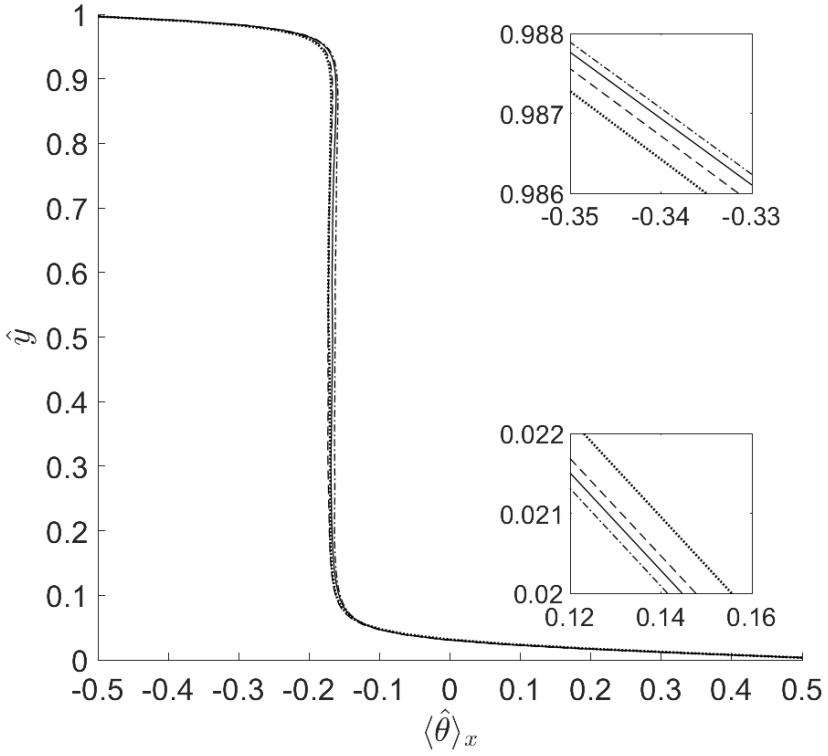

Figure 4.7: Plots of the mean normalized temperature, $\langle\hat{\theta}\rangle_x$, along the vertical direction for DNS1 to DNS4 at one lower wall temperature $T_{bot} = 315.25\,\mathrm{K}$ and for 4 ambient temperatures: $T_\infty = 289.15\,(-\cdot)$, $292.15\,(-)$, $295.15\,(--)$ and $298.15\,(\cdot\cdot)\,\mathrm{K}$.

Furthermore, at the lower bottom wall temperature, the profiles present similar slopes in the linear regions, that suggests that the ambient temperature plays a marginal role in the thermal boundary layer thickness. The $\hat{\theta}_{rms}$ profiles will be presented later on to perhaps confirm this finding. Moreover, based on the $\hat{\theta}_{rms}$ profiles' slopes in the linear regions, we observe that the dimensionless thermal boundary layer at the upper boundary $\hat{\delta}_{int}$ is thinner than at the lower boundary $\hat{\delta}_\theta$. Indeed, a sharper profile in the linear region indicates a thinner boundary layer thickness.

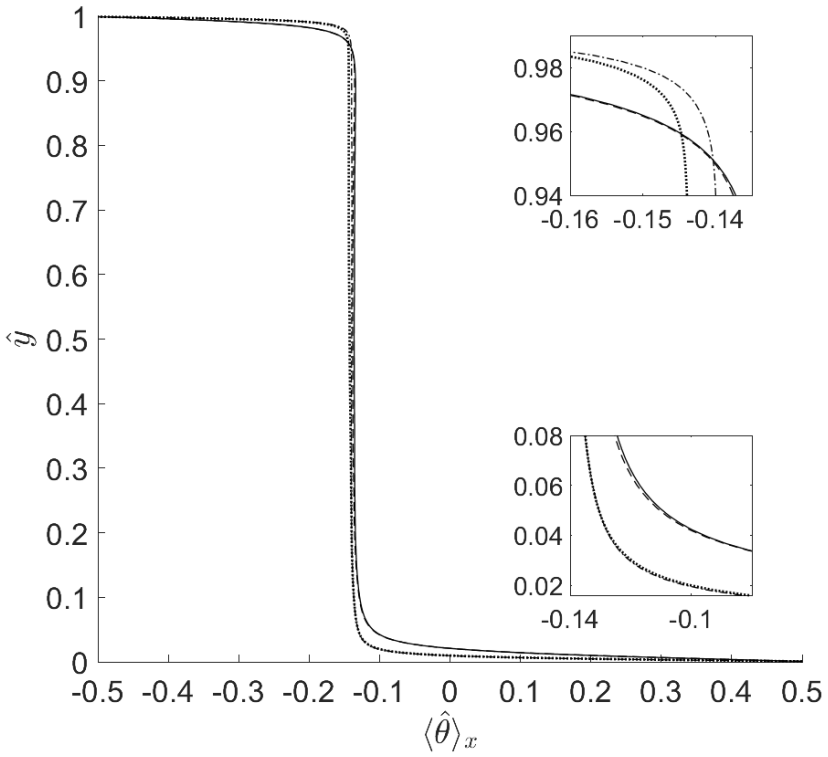

Figure 4.8: Plots of the mean normalized temperature, $\langle\hat{\theta}\rangle_x$, along the vertical direction for DNS5 to DNS8 at one lower wall temperature $T_{bot} = 345.15\,\mathrm{K}$ and for 4 ambient temperatures: $T_\infty = 289.15\,(-\cdot)$, $292.15\,(-)$, $295.15\,(--)$ and $298.15\,(\cdot\cdot)\,\mathrm{K}$.

Concerning the higher bottom wall temperature profiles, they present convergent profiles for the same pairs as for Nu_{conv}: $T_\infty = 289.15\,(-\cdot)$ & $298.15\,(\cdot\cdot)\,\mathrm{K}$ and $T_\infty = 292.15\,(-)$ & $295.15\,(--)\,\mathrm{K}$ as shown in the insets zooms of Figure 4.8. Furthermore, the profiles present significant different slopes in pairs as well which should indicate an important influence of the ambient temperature on the thermal boundary layer thicknesses. However such phenomenon would not have a physical meaning as the extreme and intermediate T_∞ considered would present similar boundary layer thicknesses. Therefore, it seems to imply a limitation of the performed 2D simulations in taking into account the impact of the complex LSC structures which differ from the diagonal plane to the orthogonal plane for $\Gamma = 1$ as it will be showed in Figure 4.21 and discussed in Section 4.2. Hence, the observed phenomenon could signify that the pairs of convergent profiles could present similar LSC structures.

We next compare the RMS of the normalised temperature fluctuations, $\hat{\theta}_{rms}$, profiles that are shown in Figure 4.9 and 4.10. We clearly observe a single peak near the lower boundary which corresponds to the lower thermal boundary layer thickness. This peak is caused by the progressive augmentation of the velocity fluctuations when moving away from the bottom wall [9]. After this peak, the profiles decrease until reaching a minimum near the centre of the domain (located at $\hat{y} = 0.5$). Contrary to what is observed in turbulent RBC, the profiles reach a maximum at the free surface. Thus, it is impossible to distinguish the profiles' upper thermal boundary layer thickness. This behaviour is caused by the free surface, which tends to increase the mean velocity at and around the upper boundary [17].

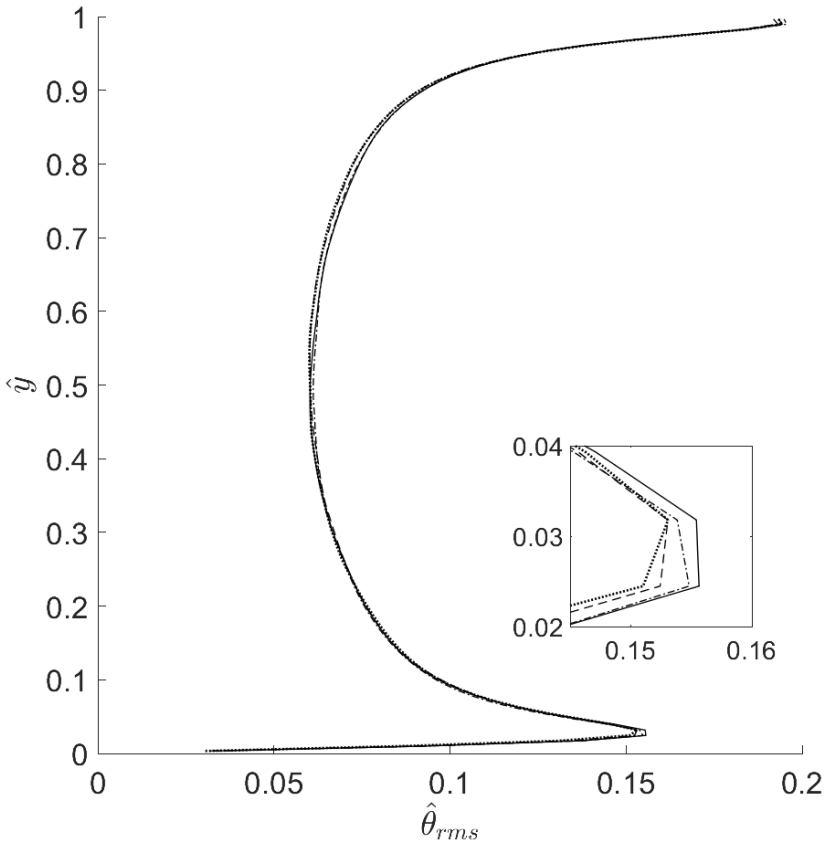

Figure 4.9: Plots of the r.m.s. of the normalized temperature fluctuations, $\hat{\theta}_{rms}$, along the vertical direction at one lower wall temperature $T_{bot} = 315.25\,\mathrm{K}$ and for 4 ambient temperatures: $T_\infty = 289.15\,(-\cdot)$, $292.15\,(-)$, $295.15\,(--)$ and $298.15\,(\cdot\cdot)\,\mathrm{K}$.

From Figure 4.9, we observe convergent profiles for the 4 different ambient conditions at $T_{bot} = 315.25\,\mathrm{K}$. The inset zoom highlights the dimensionless thermal boundary layer thickness which corresponds to the $\hat{\theta}_{rms}$ peak in the linear region close the lower boundary. It can be seen that the ambient temperature does not influence the latter as they all present the same dimensionless thermal boundary layer: $\hat{\delta}_\theta = 0.024$ which is in excellent agreement with its predicted value in Section 3.3. We do not present a method to obtain a value regarding the top boundary layer thickness as we can assume based on 4.7 that they would not differ either.

As far as the higher bottom wall temperature simulations are concerned, the phenomenon described above is again observed with the same pairs presenting convergent $\hat{\theta}_{rms}$ profiles. From the inset zoom of the Figure 4.10, 2 distinct dimensionless boundary layer thicknesses are seen: $\hat{\delta}_\theta = 0.007$ for $T_\infty = 289.15\,(-\cdot)$ & $298.15\,(\cdot\cdot)\,\mathrm{K}$ and $\hat{\delta}_\theta = 0.014$ for $T_\infty = 292.15\,(-)$ & $295.15\,(--)\,\mathrm{K}$. Such a variation is not expected, especially since it evolves in a incoherent manner with the ambient temperature, which confirms the limitation of the 2D simulations that are not adequate at high heating rates corresponding to highly turbulent flows to study a parameter which has a minor impact on the flow and its properties.

We next present the root mean square of the vertical velocity fluctuations, $\hat{v}_{rms}$, along the vertical direction. Again, the profiles are obtained for the various ambient and bottom

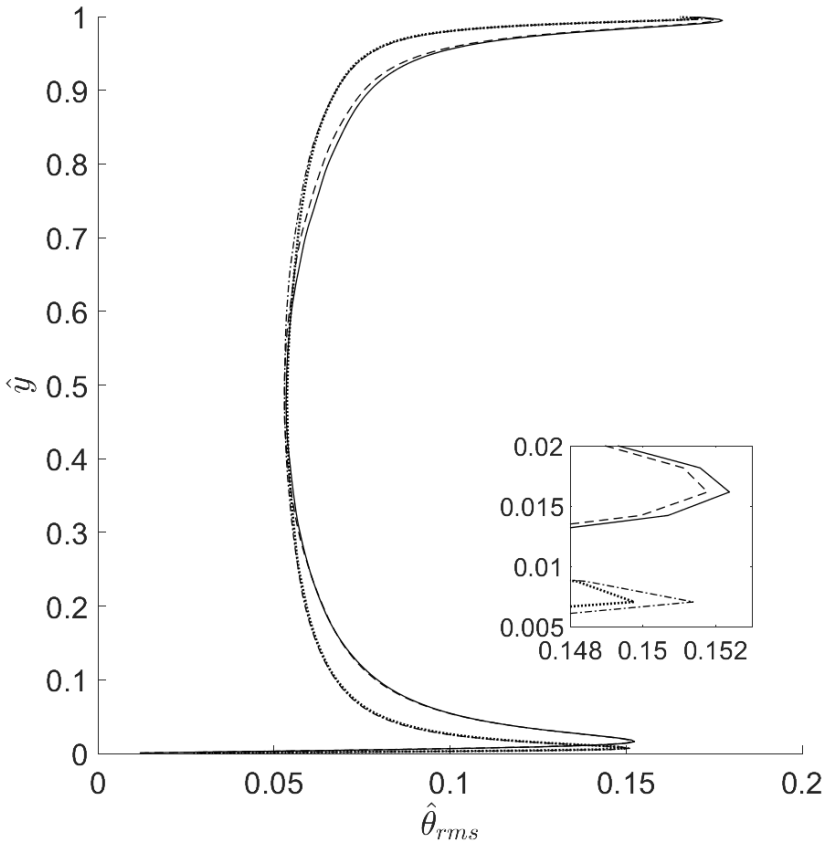

Figure 4.10: Plots of the r.m.s. of the normalized temperature fluctuations, $\hat{\theta}_{rms}$, along the vertical direction at one lower wall temperature $T_{bot} = 345.15\,\mathrm{K}$ and for 4 ambient temperatures: $T_\infty = 289.15\,(-\cdot)$, $292.15\,(-)$, $295.15\,(--)$ and $298.15\,(\cdot\cdot)\,\mathrm{K}$.

wall temperatures considered and presented in Figures 4.11 and 4.13 for $T_{bot} = 315.25$ K & $T_{bot} = 345.15$ K, respectively. From Figure 4.11 We observe that the profiles are nearly parabolic with a zero value at the bottom wall and the free surface. From these locations ($\hat{y} = 0$ & $\hat{y} = 1$), there is steep slope in the profile with a small variation in $\hat{y}$ leading to an important variation in $\hat{v}_{rms}$, a peak is is reached close the center $y \approx 0.5$. A slight asymmetry in the profiles which is due to the presence of the shear free surface is observed as in Marichal (2022) [17] and contrary to Zikanov *et al*'s symmetric profiles [31]. It also might be due to the averaging process along the horizontal axis which is affected by the left and right sidewalls' bondary layers. Concerning Figure 4.13, we observe that at the higher bottom wall temperature, the $\hat{v}_{rms}$ profiles are also affected by the limitation of the 2D simulations and present similar trends for the aforementioned pairs of ambient temperatures. It is also noticeable that the profiles have sharper slopes near the walls and higher $\hat{v}_{rms}$ peaks which means that the stirring of the fluid is enhanced compared to the lower bottom wall temperature cases. The surface-time averaged and the center Reynolds numbers: Re and Re_{ctr} are calculated based on $(\hat{v}_{rms})_{xy}$ & $(\hat{v}_{rms})_{ctr}$ which is $\hat{v}_{rms}$ at $\hat{y} = 0.5$. Re_{ctr} is defined as follows:

$$Re_{ctr} = \frac{(v_{rms})_{ctr}\, H}{\nu_{ref}}. \tag{4.11}$$

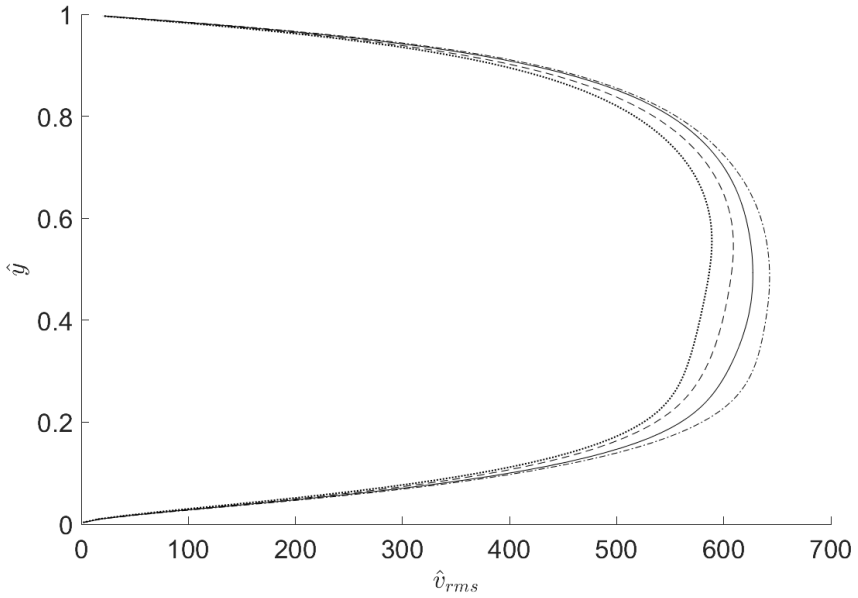

Figure 4.11: Plots of the r.m.s of vertical velocity fluctuations, $\hat{v}_{rms}$, along the vertical direction at one lower wall temperature $T_{bot} = 315.25\,\mathrm{K}$ and for 4 ambient temperatures: $T_\infty = 289.15\,(-\cdot)$, $292.15\,(-)$, $295.15\,(--)$ and $298.15\,(\cdot\cdot)\,\mathrm{K}$.

The obtained values are presented in Table 4.4 and showed in Figure 4.12 for $T_{bot} = 315.25\,\mathrm{K}$ only. From this Figure, we clearly observe a linear relationship of the Reynolds numbers with the ambient temperature. Therefore, best linear fits for Re and Re_{ctr} with respect of T_∞ are obtained from the data and provided in Eq. 4.12 & 4.13, respectively.

Case	$T_{bot}\,(\mathrm{K})$	$T_\infty\,(\mathrm{K})$	$(\hat{v}_{rms})_{ctr}$	$(v_{rms})_{xy}$ $\times 10^3(\mathrm{m/s})$	Re	$(v_{rms})_{ctr}$ $\times 10^3(\mathrm{m/s})$	Re_{ctr}
DNS1	315.25	289.15	642	1.66	117	2.17	153
DNS2	315.25	292.15	627	1.62	114	2.11	149
DNS3	315.25	295.15	608	1.57	111	2.05	145
DNS4	315.25	298.15	587	1.52	107	1.98	140

Table 4.4: Time-surface averaged and center root mean square of the vertical velocity fluctuations values and their respective Reynolds numbers for DNS1 to 4.

$$Re = -1.1\,(\mathrm{K}^{-1})\,T_\infty + 435.3, \tag{4.12}$$

$$Re_{ctr} = -1.433\,(\mathrm{K}^{-1})\,T_\infty + 567.6. \tag{4.13}$$

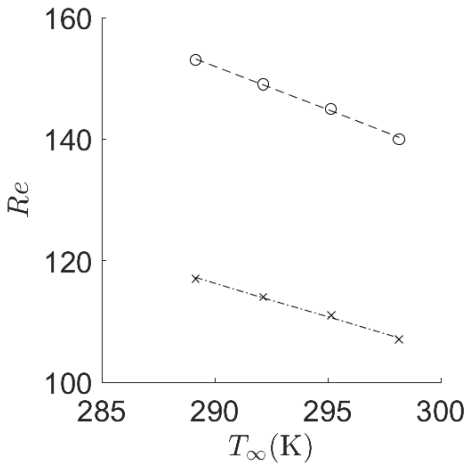

Figure 4.12: Linear fits of $Re\,(-\cdot)$ and $Re_{ctr}\,(--)$ with respect of the ambient temperature T_∞ at $T_{bot} = 315.25\,\mathrm{K}$.

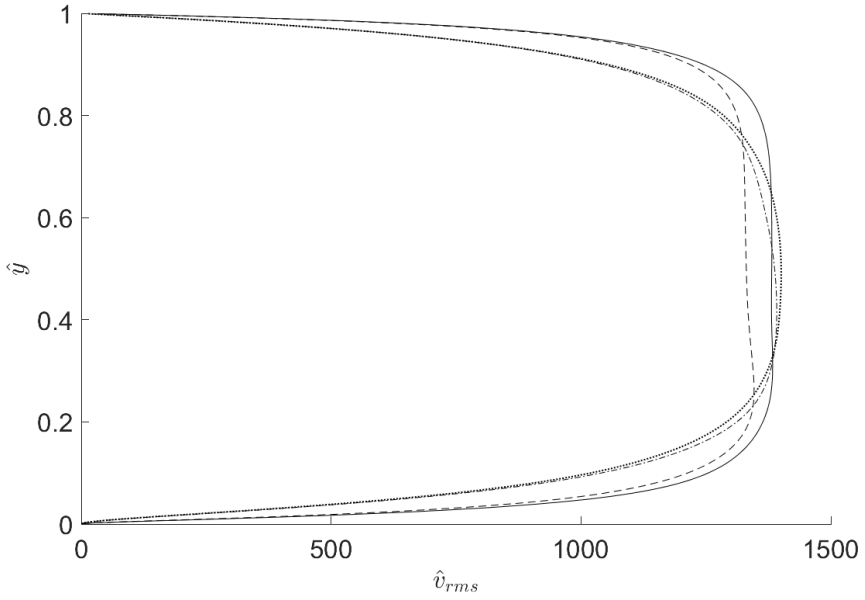

Figure 4.13: Plots of $\hat{v}_{rms}$ at one lower wall temperature $T_{bot} = 345.15\,\mathrm{K}$ and for 4 ambient temperatures: $T_\infty = 289.15\,(-\cdot)$, $292.15\,(-)$, $295.15\,(--)$ and $298.15\,(\cdot\cdot)\,\mathrm{K}$.

4.1.4 Velocity vector plots

As convergent profiles are obtained in pairs regarding the higher bottom wall temperature simulations ($T_{bot} = 345.15\,\mathrm{K}$), their respective fluid motion is investigated thanks to velocity vector plots, see Figure 4.14. From these, one can observe that DNS5 (Figure 4.14(a)) and DNS8 (Figure 4.14(d)) do not present a similar fluid motion contrary to what was expected. Indeed, an LSC almost occupies the whole DNS8 domain with secondary circulations at the bottom left and the top right while there is a global downwards motion of the fluid with bottom corner rolls regarding DNS5. Concerning DNS6 and DNS7, they present a more similar fluid motion with a LSC that take up most of their respective domain but the LSC center of DNS6 is higher resulting in a different flow feature at the bottom of its domain with an upwards

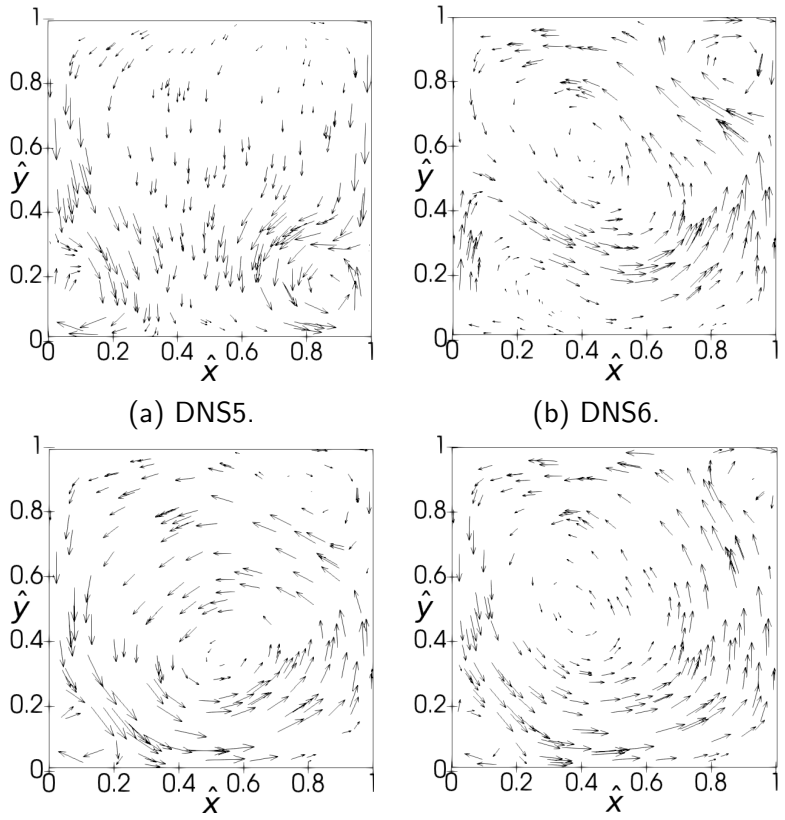

(a) DNS5. (b) DNS6.

(c) DNS7. (d) DNS8.

Figure 4.14: Velocity vector plots at the higher heating rate ($T_{bot} = 345.15\,\mathrm{K}$).

flow motion from the left corner while there is a typical corner roll at this location for DNS7. Therefore, we cannot conclude on the reason of the convergence of the profiles in pairs and further researches have to be carried out about the impact of T_∞ on fluid properties and statistic at the higher heating rate.

4.2 The influence of the aspect ratio

In this section, the influence of the aspect ratio on mean flow properties is examined considering $\Gamma = 1, 2$ and 4. Then, the role of the aspect ratio on the emerging flow patterns is investigated. For this purpose, the diagonal and orthogonal planes of the studied cuboidal domains are shown as it is known that the LSC orientates along one of them in such configuration [17]. The phenomena taking place nearby the interface are also studied thanks to contour plots of θ with superimposed velocity vectors. The same resolution requirements as DNS1 (presented in Section 3.3) are considered for the 3D simulations as well as for the free-fall time averaging period to ensure the convergence of the of the $\langle\hat{\theta}\rangle_{xz}$ and $\hat{v}_{rms}$ profiles (presented in Sections 3.6.1 and 3.6.2, respectively). This suffices considering that in 3D, mean values are obtained by averaging node values over each $x-z$ planes in the $\hat{y}$ direction instead of lines in 2D which resulting in much more averaging points.

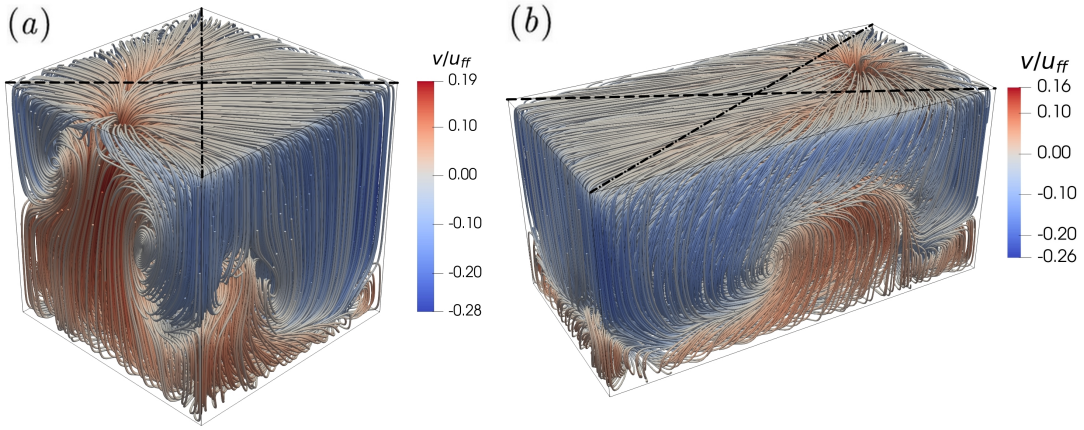

Figure 4.15: Time-averaged streamlines colored with the dimensionless vertical velocity $\frac{v}{u_{ff}}$ for: (a) $\Gamma = 1$ and (b) $\Gamma = 2$. The dashed line $(--)$ line correspond to the diagonal plane and the dash-dotted line $(-\cdot)$ to the orthogonal plane.

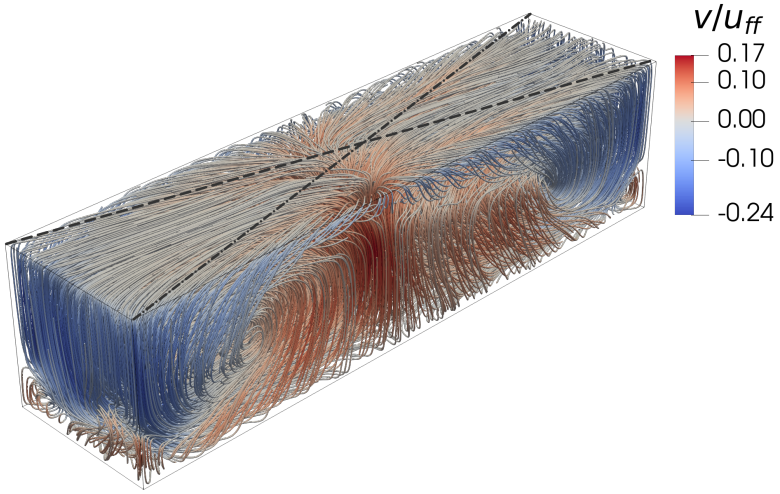

Figure 4.16: Time-averaged streamlines colored with the dimensionless vertical velocity $\frac{v}{u_{ff}}$ for $\Gamma = 4$. The dash-dotted line $(-\cdot)$ line correspond to the diagonal plane and the dashed line $(--)$ to the orthogonal plane.

Case	Ra	Γ	$T_{int}\,(\mathrm{K})$	$\Delta T_w\,(\mathrm{K})$	$\dot{m}$" $(\frac{\mathrm{g}}{\mathrm{m^2 s}})$
3D-DNS1	7.34 10^6	1	313.13	2.12	0.24
3D-DNS2	7.46 10^6	2	313.1	2.09	0.24
3D-DNS3	7.52 10^6	4	313.08	2.07	0.23

Table 4.5: Results of the simulations 3D-DNS1, 2 & 3 related to the influence of the aspect ratio Γ on the flow properties. The lower wall temperature is $T_{bot} = 315.25\,(\mathrm{K})$ for all simulations.

We first investigate the role of Γ on flow properties. The interface temperature T_{int} is obtained to calculate Ra. From Table 4.5, it can be noted that the influence of Γ on Ra is not significant. Indeed, multiplying the aspect ratio by 2 and 4 leads to relative increase of ΔT_w of about 1.4 % and 2.36 %, respectively, which is why the development concerning the influence of T_∞ on flow properties, heat transfer characteristics and flow statistics (4.1.1, 4.1.2 and 4.1.3) is not re-conducted regarding Γ. We also observe from Figure 4.17 that they present similar dimensionless boundary layer thicknesses as the slopes of the $\langle\hat{\theta}\rangle_{xz}$ profiles are similar within the linear regions at the top and bottom boundaries. Hay observed a significant impact of the aspect ratio on flow statistics and heat transfer characteristics in his study when Γ was increased through the domain's height. However, as Ra is proportional to the cube of the domain's height, it is difficult to really asses the impact of Γ on such characteristics. In the present study it, is kept constant in order to study the effect of Γ without artificially playing on it.

We then analyze the effect of Γ on the impingement location by plotting time-averaged velocity vectors superimposed with θ at $\hat{y} = 0.9965$ close to the interface in Figure 4.18, 4.19 and 4.20 for $\Gamma = 1, 2$ and 4, respectively. Impingement locations can be obtained from the highest θ point and are presented in Table 4.6 and the LSC direction can be observed thanks to the velocity vectors. We observe that the impingement location is shifted from the domain middle left to the bottom right to the top center for $\Gamma = 1, 2$ and 4, respectively. It also can be seen that the velocity magnitude progressively increases from the impingement point towards the domain's boundaries before decreasing close to them due to the applied boundary conditions.

We then turn our focus on the influence of Γ on the LSC patterns by presenting time-averaged velocity vectors with superimposed θ on diagonal and orthogonal planes for each Γ in Figure 4.21 to 4.24. The locations from which these planes are obtained are represented on time-averaged streamlines colored with the dimensionless vertical velocity, see Figures 4.18 and 4.19 where the dash-dotted line $(-\cdot)$ line corresponds to the diagonal plane and the dashed line $(--)$ to the orthogonal one. From Figure 4.21(a), one can observe the typical single-roll LSC structure that almost take up the whole diagonal plane for $\Gamma = 1$ with relatively small second structures at the top right and bottom left of the plane. It also can be seen from Figure 4.21(b) that the orthogonal plane does not present a similar flow pattern. Indeed, 2 pairs of counter-rotating vortices are observed with much larger upper vortices compared to the lower ones. To characterise their sizes, the dimensionless vertical location where the circulations interact are determined and denoted by $\hat{y}_{i,j}$, where i is for the diagonal (d) or orthogonal (o) plane and j is for the left (L) or right (R) side, their values are presented in Table 4.7. These values are obtained based on the dimensionless vertical location where there

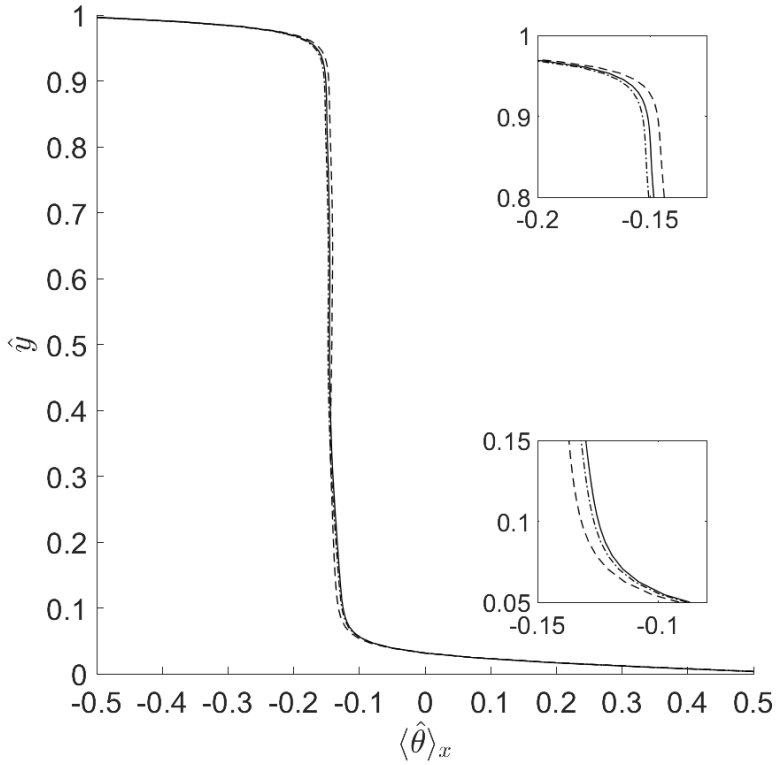

Figure 4.17: Plots of the mean normalized temperature, $\langle\hat{\theta}\rangle_{xz}$, for 3D-DNS1, 2 & 3 at one lower wall temperature $T_{bot} = 315.25\,\mathrm{K}$ and for 3 aspect ratios: $\Gamma = 1\,(-\cdot)$, $\Gamma = 2\,(-)$ and $\Gamma = 4\,(--)$.

is a change in the sign of the vertical velocity at the left and right sidewalls. From this Table, we observe that the upper LSC occupy 61 % of the plane. This phenomenon is due to the presence of the free surface which has a tendency to accelerate the flow close to the interface. This can be seen on all diagonal planes where velocity vectors pointing downwards close to the upper boundary present higher magnitude than those pointing upwards close the lower boundary.This phenomenon drives the cold fluid far downwards as it can be seen thanks to the superimposed θ contours. The cubic domain has been studied extensively in the literature and similar observations have been made [17].

Contrary to $\Gamma = 1$, the diagonal and orthogonal planes for $\Gamma = 2$ and 4 present a similar flow pattern with still one LSC that develops over the whole domain for $\Gamma = 2$ which seems to start separating into two LSC as we observe 2 LSC centers inside its structure (Figures 4.22(a) and 4.22(b)). We also observe an asymmetry between the diagonal and orthogonal planes for $\Gamma = 2$ regarding their right corner roll which is larger on the orthogonal plane compared to the diagonal one with $\hat{y}_{o,R} = 0.47$ and $\hat{y}_{d,R} = 0.32$ and is oriented upwards while it is oriented downwards on the diagonal plane. A further increase in Γ to 4 lead to the transition of the LSC from a single-roll state, in which it occupies the entire domain, to a dual-roll state as it can be seen in Figure 4.23 and 4.24 where the 2 LSC almost occupy the entire planes and with left and right bottom corner rolls. The LSC structure of both, the diagonal and orthogonal planes are this time very similar.

Γ	θ_{max}	$\hat{x}_{\theta,max}$	$\hat{z}_{\theta,max}$
1	0.06	0.13	0.48
2	0.04	1.71	0.22
4	0.03	1.93	0.85

Table 4.6: Location of θ_{max} ($\hat{x}_{\theta,max}$ and $\hat{y}_{\theta,max}$) on $x-z$ planes located at $\hat{y} = 0.9965$ for $\Gamma = 1, 2$ and 4.

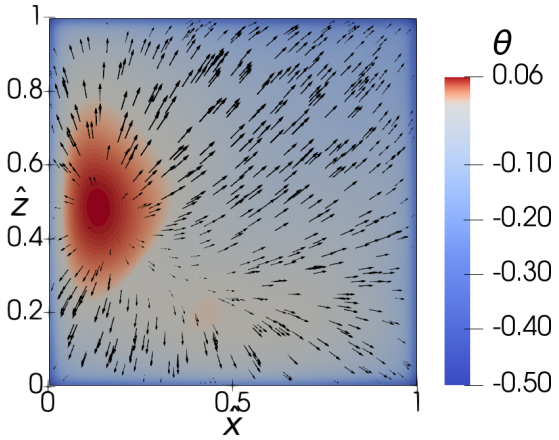

Figure 4.18: Colour plot of θ with superimposed time-averaged velocity vectors for $\Gamma = 1$ at $\hat{y} = 0.9965$.

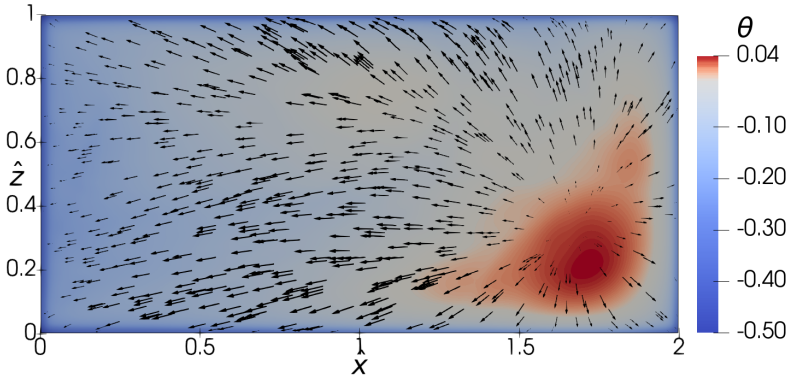

Figure 4.19: Colour plot of θ with superimposed time-averaged velocity vectors for $\Gamma = 2$ at $\hat{y} = 0.9965$.

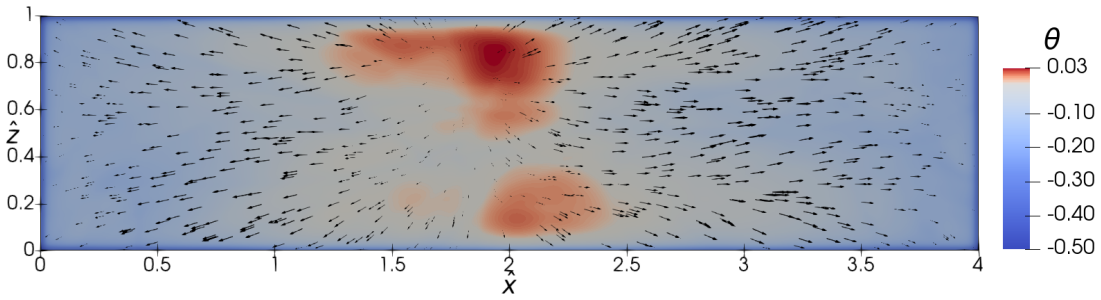

Figure 4.20: Colour plot of θ with superimposed time-averaged velocity vectors for $\Gamma = 4$ at $\hat{y} = 0.9965$.

Γ	$\hat{y}_{d,L}$	$\hat{y}_{d,R}$	$\hat{y}_{o,L}$	$\hat{y}_{o,R}$
1	0.49	0.25	0.39	0.39
2	0.33	0.32	0.31	0.47
4	0.27	0.33	0.31	0.33

Table 4.7: Dimensionless vertical recirculation limits of the diagonal (d) and orthogonal (o) planes and on the left (L) and right (R).

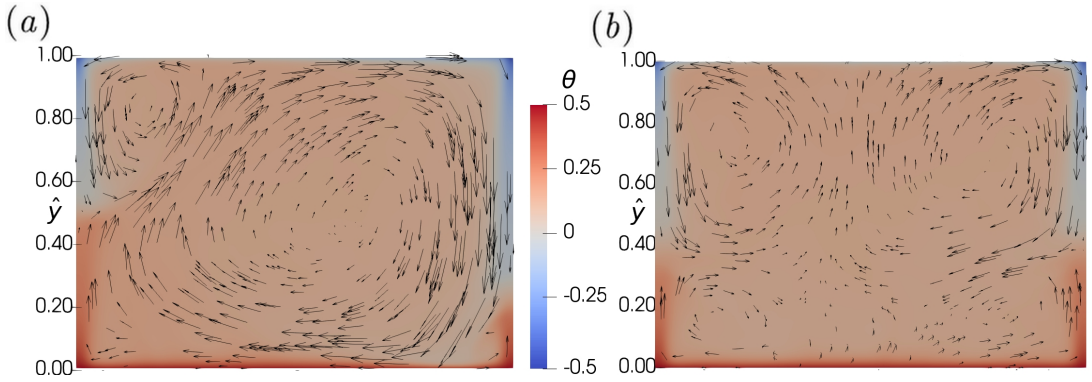

Figure 4.21: Colour plot of θ with superimposed velocity vectors for $\Gamma = 1$ of: (a) the diagonal plane and (b) the orthogonal plane.

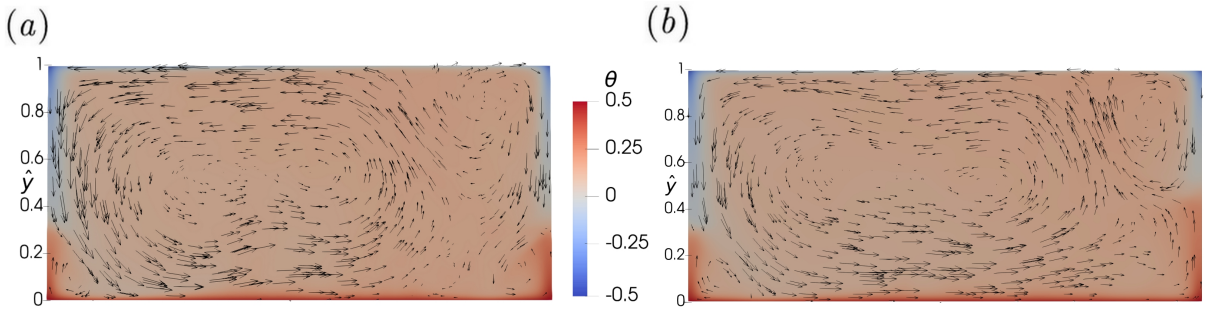

Figure 4.22: Colour plot of θ with superimposed velocity vectors for $\Gamma = 4$ of: (a) the diagonal plane and (b) the orthogonal plane.

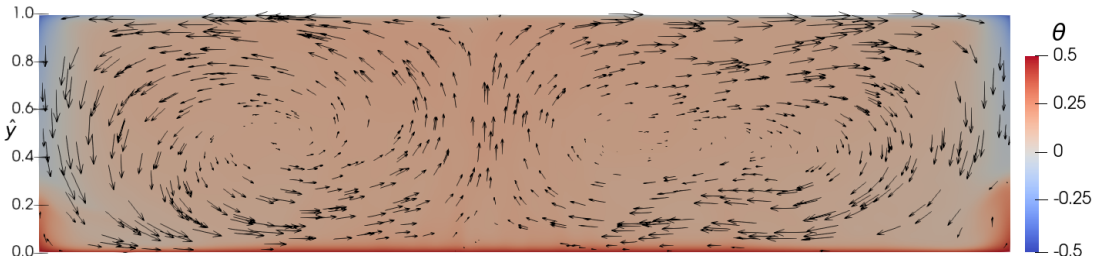

Figure 4.23: Colour plot of θ with superimposed velocity vectors for $\Gamma = 4$ of the diagonal plane.

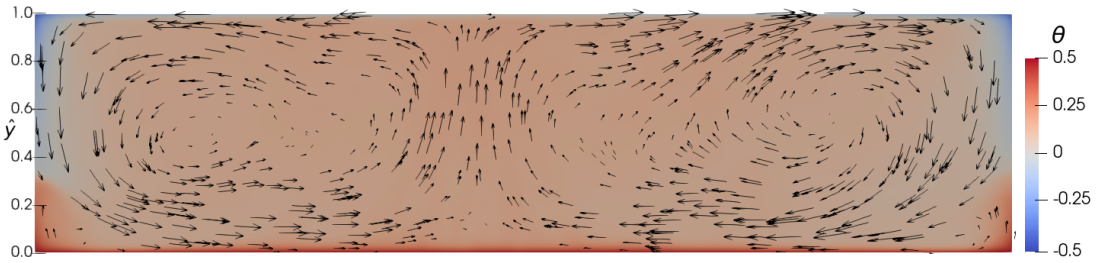

Figure 4.24: Colour plot of θ with superimposed velocity vectors for $\Gamma = 4$ of the orthogonal plane.

5 Conclusion

This paper is about turbulent thermal convection occuring in a spent fuel pool with an evaporative free surface. It started by pointing out the necessity of these water pools to store spent fuel rods which generate important amount of heat and emit radiation. Water is used in this context because it acts as a coolant and effectively blocks radiation. Then, a literature review regarding this topic was presented.

Afterwards, the hypotheses, boundary conditions, governing equations and the evaporation model were developed in Chapter 3. The main assumptions are that the spent rods which are stored in dedicated cells are replaced by a uniformly heated flat wall at the bottom of the pool, the pool side walls are considered perfectly insulated and a shear-free surface approximates the free surface. In the same Chapter, the resolution requirements to ensure that the Kolmogorov microscales are resolved everywhere within the flow were also presented. The latter consist to adequately resolve the hydrodynamic and thermal boundary layers by refining the mesh close to the walls. In this study, they are over-resolved by a factor of 2 in order to be cautious. The second requirement is related to the eddies in the bulk of the flow that have to be resolved as well and is based on a maximum cell size. After that, the convergence of mean normalised temperature, $\langle\hat{\theta}\rangle_x$, and RMS of vertical velocity fluctuations profiles, $\hat{v}_{rms}$, were presented. Ensuring the convergence of these profiles is important as interface phenomena depend greatly on the interface temperature and the investigated dimensionless heat transfer characteristics on vertical velocity fluctuations. Various averaging free-fall time periods were considered until convergent profiles were obtained indicating that a statistically turbulent steady state was reached. Only $200\,t_{ff}$ (200-400 t_{ff}) were necessary to ensure the convergence of the $\langle\hat{\theta}\rangle_x$ profiles at $T_{bot} = 315.25\,\mathrm{K}$ while 600 t_{ff} were needed at the higher bottom wall temperature $T_{bot} = 345.15\,\mathrm{K}$ (200-800 t_{ff}). The convergence of the $\hat{v}_{rms}$ profiles necessitates much longer averaging free-fall time periods, 1000 t_{ff} (200-1200 t_{ff}) for DNS1 and 1800 t_{ff} (200-2000 t_{ff}) for DNS5 were indeed needed. Therefore, the number of t_{ff} to obtain statistically steady solutions were based on the convergence of the latter as it is more strict.

The next Chapter was about the numerical results and discussion. It started with the investigation of the influences of the ambient temperature T_∞ on flow properties and statistics. For this purpose, ambient conditions in a typical ambient temperature range were considered: $T_\infty = 289.15$ to $298.15\,\mathrm{K}$ with an increment of 3 at 2 bottom wall temperatures: $T_{bot} = 315.25$ and 345.15 K. Concerning the interface temperature T_{int}, the evaporative mass flux $\dot{m}$" and Ra, linear correlations were obtained with respect to the ambient temperature.

At the higher bottom wall temperature, T_{int} and Ra evolved in a non-linear manner with respect to T_∞ but one have to be cautious about these observations as the limitation of 2D simulations to take into account the complex phenomena normally occurring in 3D were discussed. The focus was next turned on the heat transfer characteristics, consistent results were obtained at $T_{bot} = 315.25\,\mathrm{K}$ for which a decrease of the ambient temperature resulted in a substantial increase of the convective and global Nu and a linear $Nu - T_\infty$ correlation was obtained. At the higher bottom wall temperature, consistent global Nu were obtained and a linear $Nu - T_\infty$ correlation provided as well. It has also been showed that T_∞ impacts the flow properties and heat transfer characteristics in a lesser extent at the higher heating rate. Eventually, the impact of T_∞ on flow statistics was developed by comparing various profiles. The $\langle\hat{\theta}\rangle_x$ profiles showed that T_∞ does not affect the thermal boundary layer thickness at $T_{bot} = 315.25\,\mathrm{K}$, the $\hat{\theta}_{rms}$ were then presented to obtain the lower thermal boundary layer thickness. As expected, the same boundary layer height, at $T_{bot} = 315.25\,\mathrm{K}$, was obtained: $\hat{\delta}_\theta = 0.024$ and 2 different thickness were obtained at $T_{bot} = 345.15\,\mathrm{K}$ with $\hat{\delta}_\theta$ being two times thicker at $T_\infty = 289.15\,\&\,298.15\,\mathrm{K}$ than at $T_\infty = 292.15\,\&\,295.15\ \mathrm{K}$ which is not physically possible. Next, the $\hat{v}_{rms}$ profiles were presented and Reynolds numbers obtained to characterise the flow, linear $Re - T_\infty$ and $Re_{ctr} - T_\infty$ relations were proposed with Re and Re_{ctr} being negatively correlated to T_∞ at $T_{bot} = 315.25\,\mathrm{K}$. We then failed to explain the convergence of the profiles in pairs at the higher bottom wall temperature by attempting to show a similar flow motions between them.

In addition, the role of the aspect ratio Γ on the emerging LSC patterns and the impingement location was investigated by performing 3D DNS simulations with cuboidal geometries having a fixed height and width and various lengths corresponding to $\Gamma = 1, 2$ and 4. First, it was found that Γ does not seem to impact flow properties, Ra and $\dot{m}$" significantly. This can be explained as the height of the domain is kept constant and only the length is varied. Afterwards, colour plots of θ with superimposed velocity vectors were showed close to the interface at $\hat{y} = 0.9965$ and for the diagonal and orthogonal planes for each Γ. Next, the impingement location was obtained based on the peak of θ close to the free surface and we showed that it shifted from the middle left to the bottom right to the middle top for $\Gamma = 1, 2$ and 4, respectively. Finally, the LSC size were characterised by their left and right dimensionless vertical limits on the diagonal and orthogonal planes. The typical LSC pattern at $\Gamma = 1$ was discussed and it was showed that a further increase in Γ to 4 resulted in the emergence of a dual-roll state. It was also discussed that the free-surface tends to accelerate the downwards motion of the fluid close to the domain upper sides.

To conclude, consistent results were obtained regarding the role of T_∞ on flow properties and statistics at the lower bottom wall temperature but further researches are needed at the higher bottom wall temperature in particular to check the non-linear evolution of the interface temperature with respect to the ambient temperature. Dr. Carlier's current resarch at UCLouvain on simulating turbulent convection flows with intense phase change could be helpful to obtain consistent results concerning the simulations performed at $T_{bot} = 345.15\,\mathrm{K}$. Moreover, one or more assumption described in the third Chapter could be lifted in order to get closer to the real phenomena taking place in spent fuel pools.

Bibliography

[1] D. Green and C. Morris, "Nuclear spent fuel management: Experience and options: by expert groups of the nuclear energy agency oecd, paris, france, 1986, 110 pp, f150," *Land Use Policy*, vol. 5, no. 1, pp. 155–156, 1988. [Online]. Available: https://www.sciencedirect.com/science/article/pii/0264837788900221

[2] V. Etienne, "Le cycle du combustible nucléaire," *Encyclopédie de l'énergie*, Oct 2019. [Online]. Available: https://www.encyclopedie-energie.org/le-cycle-du-combustible-nucleaire/

[3] "Spent fuel management," *Diablo Canyon Decommissioning Engagement Panel*. [Online]. Available: https://diablocanyonpanel.org/decom-topics/spent-fuel-management/

[4] M. Baba, "Fukushima accident: What happened?" *Radiation Measurements*, vol. 55, pp. 17–21, 2013, 7th International Workshop on Ionizing Radiation Monitoring. [Online]. Available: https://www.sciencedirect.com/science/article/pii/S1350448713000267

[5] Q. Wang, "Turbulent thermal convection: From rayleigh-bénard convection to vertical convection."

[6] H. Jiang, X. Zhu, D. Wang, S. Huisman, and C. Sun, "Supergravitational turbulent thermal convection," *Science Advances*, vol. 6, no. 40, 2020.

[7] P. Sakievich, Y. Peet, and R. Adrian, "Large-scale thermal motions of turbulent rayleigh-bénard convection in a wide aspect-ratio cylindrical domain," *International Journal of Heat and Fluid Flow*, vol. 61, pp. 1–14, 2016.

[8] D. Lohse and K.-Q. Xia, "Small-scale properties of turbulent rayleigh-bénard convection," *Annu.Rev.Fluid Mech*, vol. 42, pp. 335–364, 2010.

[9] W. Hay, J. Martin, and M. Papalexandris, "Turbulent thermal convection driven by free-surface evaporation in cuboidal and cylindrical domains," *Physics of Fluids*, vol. 33, pp. 1–18, 2021.

[10] M. Sharif, J. Borelli, and M. Dvoracek, "Prediction of evapotranspiration using the borelli-sharif equation," *ASAE Presentation Paper*, no. 902068, 1990.

[11] M. Darwish, "Process-based aerodynamic roughness model for evaporation from free water surfaces," p. 225, 1998.

[12] J. Martin and B. Migot, "Experimental study of the surface evaporation rate of a heated water pool at high temperature using infrared thermography," *18th International Topical Meeting On Nuclear Reactor Thermal Hydraulics*, pp. 2302–2313, 2019.

[13] T. Sundari and A. Wahid, "Concentration profile and water level effect on the evaporation in the spent nuclear fuel storage pool using a diffusion approach," *IOP Conference Series Materials Science and Engineering*, vol. 1173, 2021.

[14] J. Carlier and M. Papalexandris, "An efficient tracking method for evaporative free surfaces on collocated grids," *Journal of Computational Physics*, pp. 1–30, 2022.

[15] Z. Daya and R. Ecke, "Does turbulent convection feel the shape of the container?" *Physical Review Letters*, vol. 87, no. 18-29, 2001.

[16] G. Amati, F. Massaioli, and K. Sreenivasan, "Turbulent thermal convection at high rayleigh numbers for a boussinesq fluid of constant prandtl number," *Physics of Fluid*, vol. 17(12), 2005.

[17] J. Marichal and M. Papalexandris, "On the dynamics of the large scale circulation in turbulent convection with a free-slip upper boundary," *International Journal of Heat and Mass Transfer*, vol. 183.

[18] I. Kouroudis, P. Saliakellis, and S. Yiantsios, "Direct numerical simulation of natural convection in a square cavity with uniform heat fluxes at the vertical sides: Flow structure and transition," *International Journal of Heat and Mass Transfer*, vol. 115, part B, pp. 428–438, 2017.

[19] E. Lemmon, M. Huber, and M. McLinden, "Nist standard reference database 23: Reference fluid thermodynamic and transport properties-refprop, version 9.1," 2013-05-07 2013.

[20] P. D. Antoniadis, "Time-accurate calculation of variable density flows with strong temperature gradients and combustion," Ph.D. dissertation, UCLouvain, Institute of Mechanics, Materials and Civil Engineering, 2015.

[21] B. Lessani and M. V. Papalexandris, "Modeling and numerical simulation of transient flows in superposed porous and pure-fluid layers," *Journal of Computational Physics*, vol. 212, no. 1, pp. 218–246, 2015. [Online]. Available: https://www.sciencedirect.com/science/article/pii/S0021999105003189

[22] C. M. Rhie and W. L. Chow, "Numerical study of the turbulent flow past an airfoil with trailing edge separation," *AIAA Journal*, vol. 21, no. 11, p. 1525–1532, 1983.

[23] "A new correlation method for thermodynamic data applied to the vapour pressure curves of argon, nitrogen and water: W. wagner iupac thermodynamic tables project centre (1976) 130 pp, £4," *Cryogenics*, vol. 18, no. 2, p. 122, 1978.

[24] T. R. Marrero and E. A. Mason, "Gaseous diffusion coefficients," *Journal of Physical and Chemical Reference Data*, vol. 1, no. 1, pp. 3–118, 1972.

[25] S. M. Aldarabseh and P. Merati, "An experimental investigation of the potential of empirical correlations derived based on dalton's law and similarity theory to predict evaporation rate from still water surface," *Proceedings of the Institution of Mechanical Engineers, Part C: Journal of Mechanical Engineering Science*, vol. 236, no. 12, pp. 6554–6578, 2022.

[26] J. H. Lienhard, IV and J. H. Lienhard, V, *A Heat Transfer Textbook*, 5th ed. Mineola, NY: Dover Publications, Dec. 2019.

[27] X. ZHONG, "An improved generalized watson equation for prediction of latent heat of vaporization," *Chemical Engineering Communications*, vol. 29, no. 1-6, pp. 257–269, 1984.

[28] J. R. Lloyd and W. R. Moran, "Natural Convection Adjacent to Horizontal Surface of Various Planforms," *Journal of Heat Transfer*, vol. 96, no. 4, pp. 443–447, 11 1974.

[29] O. Shishkina, R. Stevens, S. Grossmann, and D. Lohse, "Boundary layer structure in turbulent thermal convection and its consequences for the required numerical resolution," *New Journal of Physics*, vol. 12, no. 7, p. 075022, jul 2010. [Online]. Available: https://dx.doi.org/10.1088/1367-2630/12/7/075022

[30] R. Stevens, R. Verzicco, and D. Lohse, "Radial boundary layer structure and nusselt number in rayleigh–bénard convection," *Journal of Fluid Mechanics*, vol. 643, p. 495–507, 2010.

[31] O. Zikanov, D. Slinn, and M. Dhanak, "Turbulent convection driven by surface cooling in shallow water," *Phys. Fluids*, vol. 464, pp. 81–111, 2002.

UNIVERSITÉ CATHOLIQUE DE LOUVAIN
École polytechnique de Louvain
Rue Archimède, 1 bte L6.11.01, 1348 Louvain-la-Neuve, Belgique | **www.uclouvain.be/epl**